A novel multiscale design method for porous structures with tunable anisotropy: Varied-shape Voronoi tessellation

Zeyang Li, Zhangming Wu *

School of Engineering, Cardiff University, Newport Rd, Cardiff, CF24 3AA, Wales, UK

A R T I C L E   I N F O

A B S T R A C T

Natural materials, through the multiscale architected organisms they contain, can evolve and control anisotropic properties to enhance their functionality and performance, thereby improving their adaptability to external environments. Similarly, recent studies have demonstrated engineered porous materials with multiscale architected structures and tunable anisotropy can achieve superior performance compared to commonly used isotropic porous materials. In this work, by locally tessellating varied-shaped Voronoi structures with modified Riemannian metric, we develop a novel bio-inspired design framework for multiscale porous structures, which can possess tunable orientation, porosity and anisotropic property. The effective mechanical properties of multiscale varied-shaped Voronoi tessellated (VSVT) porous structures are evaluated using a numerical homogenization technique, and finally expressed as a function of design parameters, i.e., anisotropy ratio, relative density, and material direction. A gradient-based, multi-scale, multi-component optimization workflow is applied to design and optimize porous materials and structures that mimic natural patterns. Typical design cases, such as Messerschmitt–Bölkow–Blohm beams with global or local volume constraints, have been carried out to verify the proposed VSVT method. The obtained geometry models from the de-homogenization procedure not only demonstrate high computational accuracy and improved compliance performance, but also exhibit flexible biofunctional compatibility like tailored specific surface area. This implies that the proposed VSVT design method for multiscale porous materials and structures have strong potentials for engineering applications, such as, implants, architecture, energy storage, and etc.

1. Introduction

Porous materials in nature, such as diatoms, feathers, shells, bones, rocks, and wood, often possess remarkable properties in spite of their porosity and weak constituent compositions [1]. The outstanding features of natural materials, e.g., strong, tough, flexible, and lightweight, typically attribute to their ingenious hierarchical architecture, spanning from nano/micro- to macroscales. These materials with hierarchical or multiscale architecture frequently exhibit local anisotropy, wherein their properties vary depending on the direction, resulting from the alignment of internal structures, such as fibers or pores, to meet specific functional demands.

Fig. 1 shows three different biological structures: a human bone, a water lily leaf vein, and a mushroom cap, covering basic biological categories i.e. animals, plants, and fungi. Notably, all of these bio-materials share two key characteristics: multi-scale and locally varying anisotropy. "Multi-scale" means that their structures are organized at multiple levels of hierarchies. At the macro scale, the structure appears as a homogenized, continuous tissue with varying local densities, while at the micro scale,

---

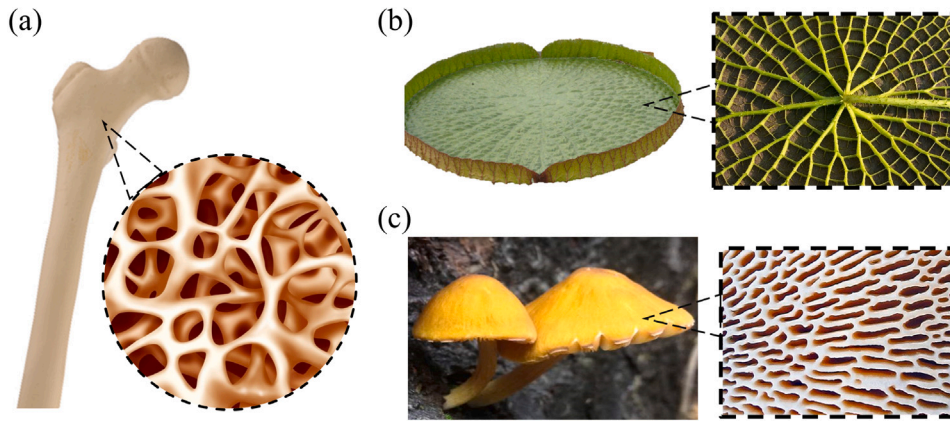**Fig. 1.** Multiscale porous (cellular) materials and structures in nature. (a) Human femoral bone with trabecular branches; (b) Water lily with its veins; (c) Fungi plant with undercover pattern. These structures are all multiscale, in which the microstructure exhibits strong anisotropy and spatially varying patterns. For example, the microstructure of the trabecular bone as (a) is usually strongly aligned with the muscle force trajectories [11]. In clinical studies, an index called 'degree of anisotropy' (DA) is used to describe the degree of heterogeneity in trabecular geometry.

it reveals a porous micro-architecture. Thus, the final mechanical properties and functionality of the entire biological material depend on the combined influence of these two levels. "Anisotropic" means that the porous micro-architecture varies in cell shape, orientation, and porosity at different spatial locations, characterized by disorder, non-uniformity, and aperiodicity. These microstructures are tailored with functionally graded properties, which thus enable the overall functionalities such as a high strength-to-mass ratio, fluid transport, energy absorption, and thermal–mechanical response [2–4]. Inspired by this, several studies have designed artificial materials using micro-scale lattices with anisotropic properties, achieving improved performance compared to those using only isotropic lattices [5,6]. Moreover, studies such as Wolff's Law for bone tissue have demonstrated that natural structures often represent the optimal design for specific mechanical or biological functions. Consequently, numerous studies have employed structural optimization as a strategy to develop bionic or bio-inspired engineering materials [7,8]. For instance, topology optimization (TO) method has been used to replicate the human trabecular bone remodeling process with high realism, achieving superior compliance performance and reduced stress shielding effects [9]. Shape optimization and evolution optimization techniques have been utilized to mimic a dragonfly wing for designing robotic flapping wing scaffold that possesses advanced aeroelasticity [10]. However, despite the success in a few examples, it is widely accepted that integrating the diverse and complex features of natural materials into a general optimization-based engineering design remains challenging, particularly when stochastic, anisotropic, and multi-scale features are required to meet, simultaneously.

To mimic the 'multi-scale' features in natural materials, multi-scale topology optimization has gained significant interests in the material design field over the past decade. This approach, leveraging multi-layer design mechanisms, offers a vast array of tailorable physical and mechanical properties for both porous materials and metamaterials [8,12,13]. 'Multi-scale' mechanism allows materials to possess with different micro-architectures and macro-spatial tessellations, thus achieving 'unique properties of micro unit cells' and 'unique functions of global structures' [14,15]. Generally, one of the key challenges in multi-scale topology optimization is overcoming high computational cost associated with the micro-scale topological model. The fundamental methodology addressing this issue is the 'homogenization-based topology optimization' proposed by Bendsøe [16], where an optimized material distribution is determined using homogenized microstructure-material properties interpolated as a function of microstructure porosity and orientation [17]. However, due to past limitations in manufacturability, this method was often sidelined in favor of other classical topology methods such as the Solid Isotropic Material with Penalization (SIMP) method [18]. In recent years, advancements in additive manufacturing techniques have overcome many traditional manufacturing limitations, making it more feasible the fabrication of much complex porous structures [19]. Consequently, there have been several attempts to revive the homogenization-based approach in multi-scale optimization. For a representative volume element (RVE) of general porous material, its elastic modulus can usually be estimated using several classical analytical homogenization methods, such as the Gibson–Ashby model [20] or Hashin–Shtrikman multiphase theory [21], when its relative density $\rho < 0.2$. Additionally, for more complex and characteristic RVE units, their elastic properties can be efficiently characterized through numerical homogenization methods [22].

However, designing porous materials with both 'stochastic' and 'anisotropic' properties within a multi-scale optimization framework remains a significant challenge. Multi-scale design methods for porous materials are generally classified into two categories: 'seed-based methods' and 'lattice embedding methods'. Seed-based methods generate a set of sampling seeds within the design domain and create topological pores at these seed locations to form the final porous structures. A notable example is the Voronoi tessellation-based design method, which applies Voronoi tessellation to create porous scaffolds with highly regular cell shapes and distributions [23–25]. Although Voronoi-based methods can achieve desirable 'stochastic' and 'non-periodic' characteristics by varying the seeding densities among different RVEs, the mechanical properties of a single RVE tend to be isotropic, limiting their ability to achieve 'anisotropic' properties. On the other hand, lattice embedding methods can easily achieve

anisotropic multi-scale designs for porous structures [26–28]. These methods define the microarchitecture using typical lattice layouts such as honeycomb, cross-truss, body-centered cubic (BCC), and Kagome [29,30], or other specifically optimized RVE architectures [26,27,31], to attain specific local anisotropic properties. The overall functionality is then achieved by optimizing the assembly of these RVEs. Although lattice embedding methods can effectively achieve the 'anisotropic' properties, they often suffer from the 'non-stochasticity' and 'connectivity' issues. Ensuring smooth connectivity between RVE interfaces typically requires additional material constraints at the boundaries, which can limit the design space and result in artificial porous patterns that lack the stochastic nature and design complexity.

Recently, innovative approaches have been developed to tackle the technical challenges of mimicking natural structures that simultaneously exhibit 'stochastic', 'anisotropic', and 'multiscale' features. Paulino et al. and Kumar et al. applied spinodal topologies to design architected porous materials with tailorable anisotropy. In their works, the material microstructure, modeled through spinodal decomposition theory with specific porosity and orientation, achieves tuned local anisotropy at the micro-level while maintaining excellent connectivity and randomness over the entire design domain [5,32]. However, this method may generate isolated flaws in designed porous structures, and the final complex topological manifold due to its high-curved boundary surfaces also poses certain challenges for manufacturability. On the other hand, some researchers began to design porous structures through modified Voronoi cells, which typically have relatively simple manufacturing requirements due to their "quasi-convex pores" or "truss-based structure" geometrical features. Ying et al. [6] pioneered an advanced approach for designing anisotropic porous structures using anisotropic centroidal Voronoi tessellation. With their approach, the standard Voronoi cell is transformed into a 'stretching' form to present anisotropic properties. Liu et al. [33] further developed Ying's work by applying a stress field leading design method to decide the shape and location of their Voronoi cells. This approach enhances the final performance of the tailored porous architecture. However, the overall framework in the context remains at a qualitative design level rather than a numerical structural optimization, lacking precise compliance calculations or volume constraints. To make further progress in this field, there remains a need to develop a comprehensive optimization framework for multiscale porous structures with tunable anisotropy.

In this work, we introduce a novel multi-scale structural optimization approach utilizing varied-shape Voronoi tessellation (VSVT) to design truss-based porous materials and structures, for which both local anisotropic micro-architecture and overall optimized functionality are allowed for the tunability. This proposed bio-inspired design method mimics several microstructural characteristics observed in nature, e.g., trabecular, coral skeleton and rock. As such, it not only can achieve a superior mechanical performance and lightweight features, but also has a good potential to promote other functionalities through its diverse porosity and micro-architecture tessellation. Specifically, a varied-shape Voronoi tessellation (VSVT) method is firstly proposed for designing anisotropic porous micro-structures with respect to three predefined design variables, i.e., anisotropy ratio, relative density, and angle parameters. Then, the VSVT structure is numerical homogenized to derive its elasticity tensor function to the design variables. A multi-component VSVT design method using homogenized FE elements is employed to find the optimal solution for porous structures with maximized mechanical performance. The resulting solutions demonstrate significantly superior compliance performance compared to existing isotropic porous designs. In addition, the de-homogenization process of obtaining target micro-structural architectures in the VSVT method is accurate and flexible. The proposed structural optimization exhibits excellent geometry-tailoring capabilities and effectively adheres to local volume constraints. It is expected that this work will provide an efficient tool for designing porous materials and structures in practical engineering applications, e.g., foam alloy, bone implant and energy storage devices, etc.

The section of this article is organized as follows: Section 2 introduces the design framework of porous structure by Varied-shape Voronoi Tessellation (VSVT) method and corresponding anisotropic material property; The corresponding optimization method and de-homogenizing process is also introduced in this section. Section 3 introduces the numerical example for the VSVT structure to verify the proposed method. The comprehensive discussions and conclusions are presented in Section 4.

2. Methods

This section introduces the detailed optimization process of the proposed method for constructing a VSVT porous structure. The entire workflow is divided into two stages: 'modeling part' and 'optimization part', as shown in Fig. 2. The related variables and parameters in the process are also marked in the flowchart. It is notable that, in this work, the design variables for the VSVT structures and the parameters for topology optimization are not completed equal but have a mapping relationship, as shown in Fig. 2. Numerical homogenization and de-homogenization techniques were used to complete above matching process.

2.1. Porous materials design by varied-shape Voronoi tessellation (VSVT) method

Given a specific set of seeding points $\{\mathbf{P}_k\}$, Voronoi tessellation divides the spatial domain Ω into several Voronoi cells, each of which corresponds to a unique Voronoi seed. For each Voronoi cell R_k, its inner points are closest to its own Voronoi seed compared to any other Voronoi seeds, as:

$$R_k = \{\mathbf{x} \in \Omega | d(\mathbf{x}, \mathbf{P}_k) \leq d(\mathbf{x}, \mathbf{P}_j)\}, \qquad \text{for all } j \neq k \tag{1}$$

where j, k are the indices of Voronoi seeds, $d(\mathbf{x}, P_k)$ is the distance function of Voronoi tessellation. The standard Voronoi tessellation is constructed based on Euclidean distance, as follows,

$$d(\mathbf{x}, \mathbf{P}_k) = \|\mathbf{x} - \mathbf{P}_k\|_2 = \sqrt{(x - x_{pk})^2 + (y - y_{pk})^2} \tag{2}$$
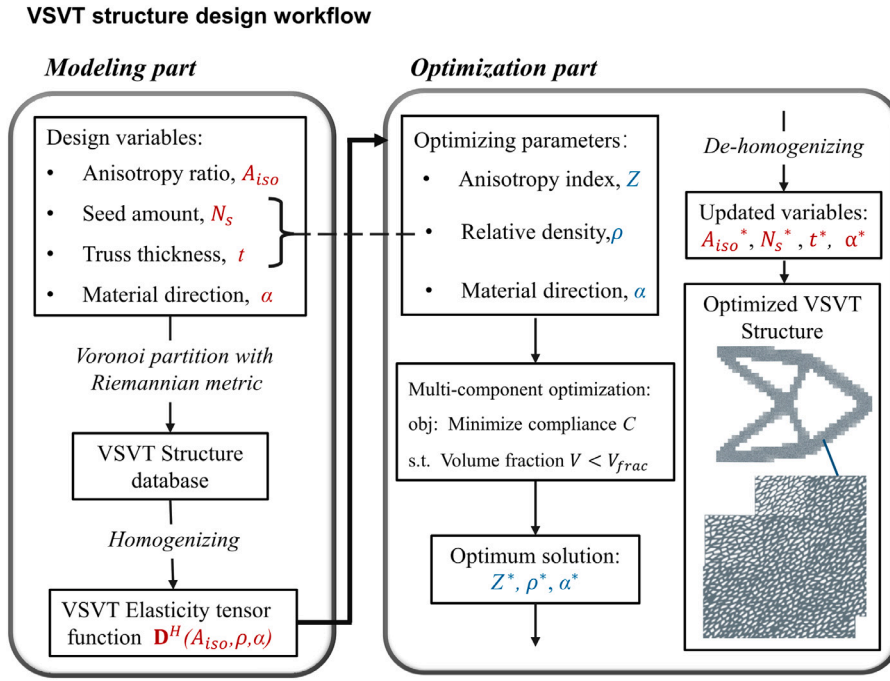
VSVT structure design workflow

Fig. 2. The complete workflow demonstrating the design process of VSVT porous structure.

where x, y, x_{pk}, y_{pk} are the corresponding spatial coordinates of point $\mathbf{x}$ and Voronoi seed $\mathbf{P}_k$, respectively. With this definition, the pore shapes tend to exhibit a stochastic, quasi-pentagon or hexagon pattern once the Voronoi seeds are uniformly stochastic distributed in the space, as depicted by Fig. 3(a). Previous studies have demonstrated that these porous structures constructed using standard Voronoi tessellation exhibit overall isotropic mechanical properties after performing the homogenization process [23,24, 33].

Notably, the distance function $d(\mathbf{x}, \mathbf{P}_k)$ plays a critical role in deciding the partition pattern of a Voronoi tessellation. In view of this, the distance function $d(\mathbf{x}, \mathbf{P}_k)$ is able to be artificially modified to construct novel Voronoi cells, whose shapes can vary in desired directions. For the sake of simplification, we mainly construct VSVT structures with quasi-orthogonal anisotropic characteristics in this work, through a varied distance function $\tilde{d}(\mathbf{x}, \mathbf{P}_k)$ defined as,

$$R_k = \{\mathbf{x} \in \Omega | \tilde{d}(\mathbf{x}, \mathbf{P}_k) \leq \tilde{d}(\mathbf{x}, \mathbf{P}_j)\}, \qquad \text{for all } j \neq k \tag{3}$$

while

$$\begin{cases} \tilde{d}(\mathbf{x}, \mathbf{P}_k) = \|\mathbf{A}_{iso}\mathbf{R}(\mathbf{x} - \mathbf{P}_k)\|_2 \\ \mathbf{x} = \begin{pmatrix} x, & y \end{pmatrix}^T, \qquad \mathbf{P}_k = \begin{pmatrix} x_{pk}, & y_{pk} \end{pmatrix}^T \\ \mathbf{R} = \begin{bmatrix} \cos\alpha & \sin\alpha \\ -\sin\alpha & \cos\alpha \end{bmatrix}, \qquad \mathbf{A}_{iso} = \begin{bmatrix} 1 & 0 \\ 0 & A_{iso} \end{bmatrix} \end{cases}$$

where $\mathbf{R}$ and $\mathbf{A}_{iso}$ named as the coordinate rotation matrix and the anisotropy matrix. A_{iso} is a predefined index, namely the anisotropy ratio, which quantitatively represents the degree of anisotropy of a VSVT structure. Herein, the $\tilde{d}(\mathbf{x}, \mathbf{P}_k)$ in Eq. (3) is no longer a Euler distance but designed by specialized Riemannian metric. At this stage, the two spatial coordinates of the vector $\mathbf{x} - \mathbf{P}_k$ along the x- and y-axes exert an unequally weighted influence on the final modified distance $\tilde{d}$ in Eq. (3) depending on its value of A_{iso}. Consequently, the Voronoi cells in the design domain finally exhibit a 'stretching' effect along a specific direction, resulting in shapes that are more elongated rhomboids rather than regular hexagons or pentagons, as illustrated in Fig. 3(b) and (c). This induces significantly different volume fractions of struts along the orthogonal axial directions x', y' in the spatial space, thus, the new VSVT pattern is predictable to exhibit heterogeneous mechanical properties in both of directions. Furthermore, by applying the rotation matrix $\mathbf{R}$ with an angle parameter α, the principal direction of the VSVT material properties can be further adjusted as shown in Fig. 3(c).

Given a specific seeding set, the vertex coordinates of each slender rod in VSVT Voronoi cells can be determined uniquely from Eq. (3). As such, the scaffolds of the Voronoi cells are defined, and one can assign the thickness on them to completely generate a 2-D solid truss-based porous structure. Herein, we use a geometric mapping function (the level-set method) to describe the practical material phase field of the VSVT porous model. The vertex coordinates of ith truss bar in VSVT structure as a $\{(x_{i,1}, y_{i,1}), (x_{i,2}, y_{i,2})\}$.
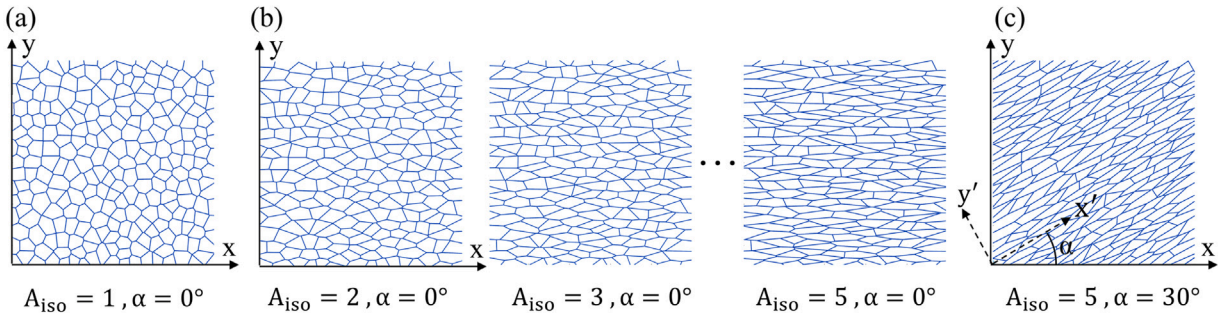
Fig. 3. VSVT porous structures with respect to different design variables, i.e., anisotropy ratio A_{iso} and material principal direction α. (a) The isotropic porous structure corresponds to the standard Euclidean distance function $d(\mathbf{x}, \mathbf{P}_k)$ in Eq. (1). (b) and (c) represent a series of anisotropic porous structures corresponding to modified distance function $\tilde{d}(\mathbf{x}, \mathbf{P}_k)$, as given in Eq. (3). Notably, all of the VSVT structures in this figure share the same voronoi seed set $\{\mathbf{P}_k\}$.

The material phase of a typical VSVT structure, Ω is stated as,

$$
\begin{cases}
\phi(\mathbf{x}) > 0, \mathbf{x} \in \Omega \\
\phi(\mathbf{x}) = 0, \mathbf{x} \in \partial\Omega \\
\phi(\mathbf{x}) < 0, \mathbf{x} \in S_D \setminus \Omega
\end{cases}
, \text{ where }
\begin{cases}
\phi(\mathbf{x}) = \max(\phi_{i,r}(x,y,t), \phi_{i,c1}(x,y,t), \phi_{i,c2}(x,y,t)) \\
\phi_{i,r}(x,y,t) = \min(\phi_{i,r1}(x,y,t), \phi_{i,r2}(x,y,t)) \\
\phi_{i,r1}(x,y,t) = 1 - \frac{(-\sin(\theta)\cdot(x-x_{i,0})+\cos(\theta)\cdot(y-y_{i,0}))^2}{(t_i/2)^2} \\
\phi_{i,r2}(x,y,t) = 1 - \frac{(\cos(\theta)\cdot(x-x_{i,0})+\sin(\theta)\cdot(y-y_{i,0}))^2}{(L/2)^2} \\
\sin(\theta) = \frac{y_{i,2}-y_{i,1}}{L}, \quad \cos(\theta) = \frac{x_{i,2}-x_{i,1}}{L} \\
x_{i,0} = \frac{x_{i,1}+x_{i,2}}{2}, \ y_{i,0} = \frac{y_{i,1}+y_{i,2}}{2}, \\
L = \sqrt{(x_{i,2}-x_{i,1})^2 + (y_{i,2}-y_{i,1})^2} \\
\phi_{i,c1}(x,y,t) = 1 - \frac{(x-x_{i,1})^2+(y-y_{i,1})^2}{(t_i/2)^2}, \\
\phi_{i,c2}(x,y,t) = 1 - \frac{(x-x_{i,2})^2+(y-y_{i,2})^2}{(t_i/2)^2}
\end{cases}
\tag{4}
$$

where $\partial\Omega$ is the boundary of the solid geometry of the VSVT structure. S_D is the region of the total design space, and $\mathbf{x}$ is the coordinate vector of S_D. The default 2-D topological shape of the ith truss component contains a rectangular body and two circle endpoints corresponding to function $\phi_{i,r}(x,y,t)$, $\phi_{i,c1}(x,y,t)$ and $\phi_{i,c2}(x,y,t)$, respectively. θ is the angle of inclination of the truss body with respect to the positive direction of the x axis and its corresponding trigonometric values are expressed as 'sin(θ)' and 'cos(θ)' terms in the equation. t_i is the given thickness value of the truss component. The complete VSVT structure is finally obtained through a Boolean merging operation of the rectangular and circular regions of all truss components. This is accomplished using a 'max' operation on the terms $\phi_{i,:}$ in Eq. (4).

In existing works, the uniform, homogeneous distribution for the seeding set in the design space (RVE) typically suggests an equal seeding density across the area. This can be achieved using several sampling methods, including Poisson-Disk, Blue Noise, Halton Sequence and Monte Carlo sampling. In this work, Bridson's Poisson Disk sampling method [34,35] is applied to generate Voronoi seeds with stochastic features, closely resembling natural structures. In doing so, it enhances the bio-similarity in the design of VSVT structures. The detailed seeding process using the Poisson Disk sampling method is presented in Appendix A. For each RVE in a normalized size of 1×1, a threshold range for the number of seeding points $N_s \in [60, 120]$ is set in the work to ensure the generation of sufficiently dense Voronoi cells within the domain. In doing so, the influence of geometric randomness on the properties of the RVE is significantly reduced. Consequently, the volume and elasticity tensor of the RVE can be accurately expressed as functions of the design variables through homogenization computation.

2.2. Homogenization of VSVT micro-structures

Firstly, it is important to determine the effective Young's modulus of the proposed VSVT micro-structure and study its anisotropic effects. The macroscopic effective elasticity tensor, E_{pqrs}^H, of some typical VSVT micro-structures (RVEs) with respect to different design variables is determined using a homogenization process. The aim of this subsection is to establish the matching relationship between effective Young's modulus (elasticity tensor) and the three design parameters of VSVT porous structures, i.e., anisotropy ratio A_{iso}, relative density ρ, and material principal direction α. For the sake of simplification, the default size of each RVE unit is set as 1×1, and the Young's modulus and Poisson's ratio of the basic material are set as $E_s = 1$ and $v = 0.3$, respectively. Therefore, the 'effective modulus' of the material E^H/E_s is simplified as E^H. The normalized thickness t/L_{RVE} and the relative seeding density N/S_{RVE} can also be directly equal to the thickness t and the number of seeds N_s.

Regarding a general cellular structure under the periodic boundary condition, the macroscopic effective elasticity tensor, E_{pqrs}^H, of a single RVE is determined using a homogenization process, and expressed as [22,25],

$$E_{pqrs}^H = \frac{1}{V} \int_{\Omega_{RVE}} E_{pqrs} \left(\varepsilon_{ij}^{0(pq)} - \varepsilon_{ij}^{pq} \right) \left(\varepsilon_{kl}^{0(pq)} - \varepsilon_{kl}^{pq} \right) dV \tag{5}$$

where V is the volume of a RVE element and takes a normalized value 1. $\varepsilon_{ij}^{0(pq)}$ is the prescribed macro-scale strain function and ε_{ij}^{pq} is the local varying elasticity field. For the sake of simplification, we assume $\varepsilon_{ij}^{0(pq)}$ equal unit strain boundary $\varepsilon_{ij}^{0(11)} = \{1,0,0\}^T$, $\varepsilon_{ij}^{0(22)} = \{1,0,0\}^T$, and $\varepsilon_{ij}^{0(12)} = \varepsilon_{ij}^{0(21)}\{1,0,0\}^T$ as the basic boundary conditions. In the meanwhile, the term ε^{pq} is calculated through a detailed 2D FEM model of VSVT truss structures under a *plane-stress* state. By solving Eq. (5), the final homogenized elasticity tensor E_{ijkl}^H is obtained and expressed in form of a Voigt notation as,

$$\mathbf{D}^H = \begin{bmatrix} D_{11} & D_{12} & D_{13} \\ D_{21} & D_{22} & D_{23} \\ D_{31} & D_{32} & D_{33} \end{bmatrix}, \text{ while } D_{ij}^H = D_{ji}^H \tag{6}$$

where D^H is a symmetric matrix which usually contains six independent elements for a general heterogeneous material. The subscripts $1, 2, 3$ correspond x, y, z axis direction in the Cartesian coordinate system, respectively. Specifically, if a RVE structure possess an orthotropic mechanical property, the number of independent terms in the elasticity tensor will decrease to be 4, as D_{11}, D_{22}, D_{12}, D_{33}, and $D_{13} \equiv 0, D_{23} \equiv 0$. Under a 2-D *plane stress* state, the effective Young's modulus of the homogenized element is evaluated as $E_x = 1/S^H(1,1), E_y = 1/S^H(2,2)$, which are the corresponding Young's modulus along x, y-axis directions, respectively. S^H is the flexibility matrix as the inverse of D^H, i.e., $S^H = [D^H]^{-1}$.

2.3. Mechanical properties of VSVT RVE units

This section presents the mechanical properties of VSVT RVE units, e.g. relative density property, homogenized elasticity. Although VSVT is a typical stochastic porous material, its micro-architecture over a local domain possesses a strong regularity. This feature allows us to design VSVT structures (RVEs) that possess tunable yet stable anisotropic mechanical properties. From a design perspective, it is widely accepted that the stochastic influence of the micro-architecture of a porous material significantly decreases once the total number of pore cells surpasses a certain threshold in the design domain. At this point, the mechanical properties or volume property of the RVE unit of a porous material are usually stable and strongly correlated with its design variables [36]. Numerous isotropic Voronoi-based porous structures have validated this observation, explicitly determining the elasticity tensor or Young's modulus of RVE units as a polynomial or exponential function in terms of the relative density, ρ, in accordance with the Gibson–Ashby theory [36].

In the optimization process, the effective Young's modulus E^H of a RVE unit is usually evaluated in terms of its relative density 'ρ', as discussed in Section 2.1. Here, the relative density ρ is defined as the ratio of the inner solid material volume to the total volume of a single RVE unit. Obviously, the value of ρ will be determined by N_S and t, jointly. To derive the accurate mapping relationship between the relative density ρ and N_S, t, a database of VSVT RVE units was constructed through the combinatorial configurations by varying N_s from 10 to 200, t from 0.01 to 0.1 and A_{iso} from 1 to 5, respectively. For each set of design parameters (e.g., $N_s = 10$ and $t = 0.05$ under $A_{iso} = 1$), 10 repetitive VSVT models are generated, and their corresponding material properties are determined. Subsequently, by performing the statistic analysis of each dataset, the influence of the stochasticity of the VSVT structure on its elastic properties is quantitatively analyzed.

The variations of the relative density ρ with respect to N_S and t are derived and depicted in Fig. 4(a) and (b), which corresponding the cases of $A_{iso} = 1$ and $A_{iso} = 5$, respectively. It is observed that ρ approximately follows a quasi-exponential function with respect to N_s or t. The dispersion error of ρ rapidly decreases as the number of seeds N_s increases. The maximum 'Deviation Rate' for ρ is of 19.6% and 15.0% for cases (a) and (b), respectively, both of which occur at the data curve of $N_s = 10$, $t = 0.05$. When N rises to 60, the 'Deviation Rate' rapidly decreases to 3.9% and 2.3% for cases (a) and (b), respectively. The standard variation is 0.0278 and 0.04 for cases (a) and (b), respectively, when $N = 10$. In comparison, these values decrease to 0.007 and 0.004 when N increase to 60. Based on this preliminary validation, we conclude that an implicit function $\rho(N_s, t)$ that can accurately map the relative density (ρ) to the design parameters (N_s, t) exists for VSVT structures, when N_s is in the interval of [60, 200].

Considering the manufacturability and practical applications, this study mainly focuses on the design variables within the ranges of $\rho \in [0.2, 1]$ and $N_s \in [60, 120]$ in subsequent sections. A small-scale double-layer feed-forward network (DFN) rather than the polynomial fitting function is used to explore the implicit mapping function $\rho(N_s, t)$. N_s and t are defined as the basic input of DFN, while ρ is set as the output. The hidden layer amount and training-validation split ratio is respectively set as 5 and 75%:25%. The training process was completed using MATLAB neural network fitting toolbox (version 23, Mathworks.co., Ltd). The method yielded a curved interpolation surface with high efficiency and accuracy as depicted in Fig. 4(c) and (d). The training process on a 400-sample database was completed within 2 s and the mean squared error (MSE) for the curve fitting is less than 1e-5. This trained DFN and the generated data will be used for the de-homogenization process of this work.

To further study the mechanical properties of VSVT RVE units, in particular their anisotropic effects, we analyze the effective Young's modulus of VSVT RVE units with different configurations that are extracted from the database. The curve fitting results clearly demonstrate the mapping relationship between the effective modulus and the design variables, i.e., A_{iso}, ρ and α. Fig. 5(a) illustrates the variations of effective Young's modulus E_x and E_y with respect to the relative density ρ under different values of A_{iso}.
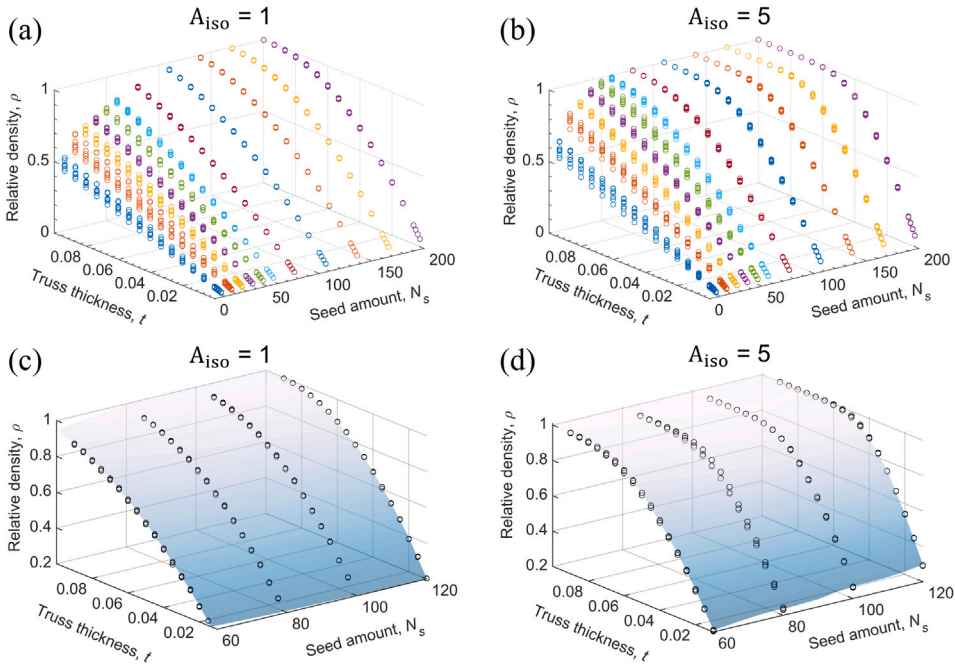
Fig. 4. The mapping relationship of ρ with respect to seed amount N_s and truss thickness t for various VSVT structures (RVEs). (a) and (b) present data curves with $N_s \in [10, 200]$ under $A_{iso} = 1$ and 5, respectively. (c),(d) presents the predicted neural network function as blue-white surface for $N_s \in [60, 120]$ and $\rho \in [0.2, 1]$ $A_{iso} = 1$ and 5, respectively. The average error of the predictions for both cases is under 1%.
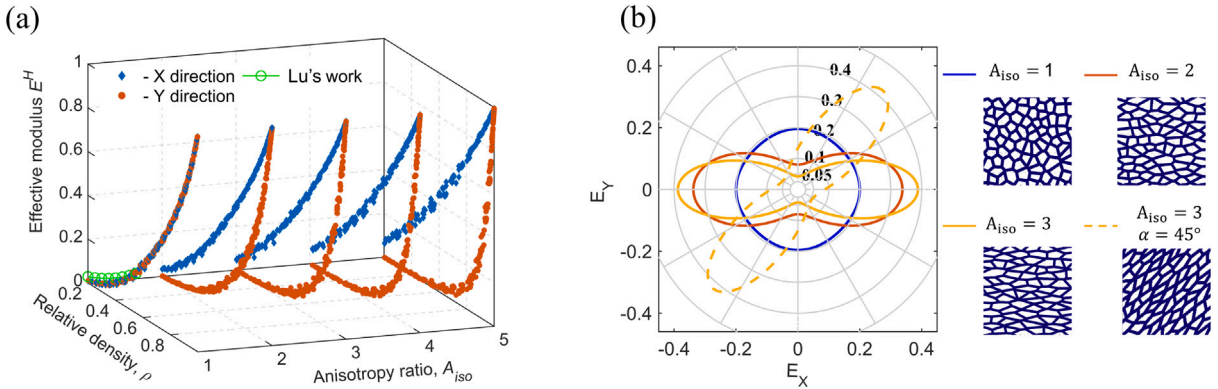

Fig. 5. The demonstration of effective modulus for VSVT RVEs with different configurations. (a) shows the Young's modulus of the RVE in X- and Y- direction (as Fig. 3) while $A_{iso} = 1, 2, 3, 4, 5$ and $\rho \in [0.2, 1]$. The curve $A_{iso} = 1$ represent a isotropic material state. This data is closed with ones by Lu's study [23] which is illustrated as the green 'o' curve. (b) presents polarized plots of effective modulus for four typical VSVT RVE. The corresponding shows clear isotropic or orthotropic characteristic. The fourth RVE is set as $\alpha = 0°$, while others $\alpha = 0°$.

It shows that the effective modulus E_x or E_y both exhibit a clear power function relationship with respect to the relative density ρ under the same A_{iso}. When $A_{iso} = 1$, the VSVT method, which corresponds to a normal Euclidean distance function, results in a standard Voronoi-tessellated porous architecture. In this case, it leads to the RVE unit to possess an approximate isotropic elasticity tensor, for which the Young's modulus curves of 'E_x' and 'E_y' are almost the same, as shown in Fig. 5(a). This finding is consistent with the results for Voronoi-based isotropic porous materials by Lu et al. [23], depicted by the green curve in the image.

As A_{iso} gradually increases from 1 to 5, the geometry of the VSVT cellular structure exhibits a strong stretching effect along the x-axis. This architecture results in a nonequivalent material distribution in the x and y directions, which well explains why E_x increases significantly while E_y decreases to some extent in Fig. 5(a). Fig. 5(b) illustrates the polar plots of the elasticity tensor for four VSVT RVE units with different configurations as, A_{iso}, ρ, α = (1, 0.5, 0°), (2, 0.5, 0°), (3, 0.5, 0°), (3, 0.5, 45°). The corresponding modulus values align with the aforementioned statements. Furthermore, the VSVT RVE units with $A_{iso} = 1$ or $A_{iso} = 2, 3$ (with $\alpha = 0°$) exhibit a strong isotropic or orthotropic characteristic, respectively. While, the VSVT structure with $\alpha = 45°$ exhibits a strong anisotropic
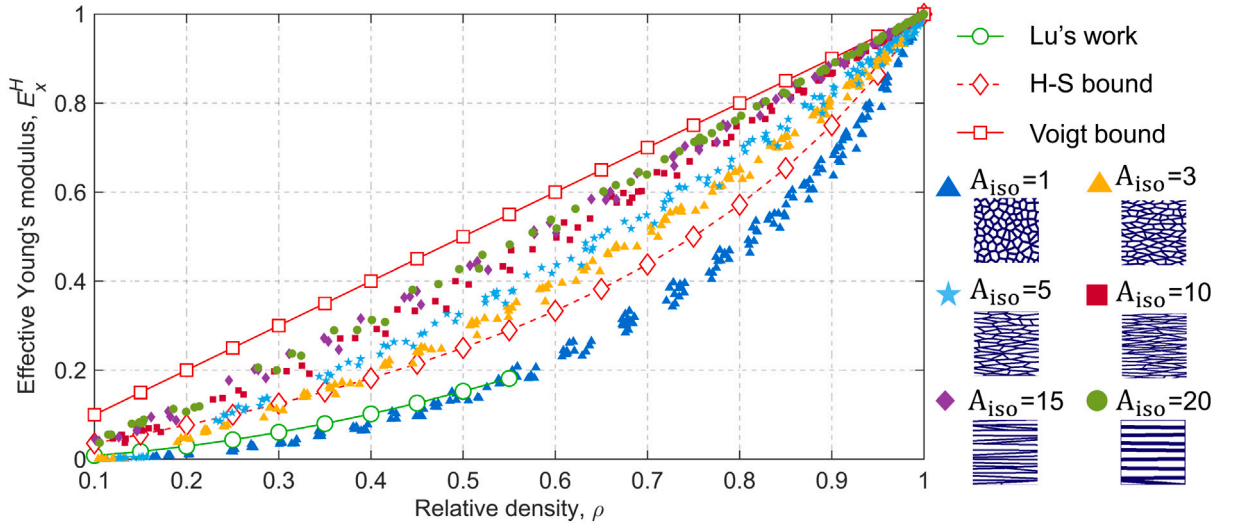
Fig. 6. The demonstration of homogenized Young's modulus E^H with respect to the anisotropy ratio $A_{iso} = 1, 3, 5, 10, 15, 20$. As A_{iso} increases, the pattern of VSVT porous structure will gradually transform into parallel strip architecture, while its material strength exceeds the H–S (Hashin–Shtrikman) bound and approaches the Voigt bound. For the sake of clarity, the actual seed amount N_s of the right side RVE decreases from 60 to 45, 30, and 10 for the cases of $A_{iso} = 10, 15$, and 20, respectively.

effect. Note, A_{iso} is not necessary to be an integer and can be a continuous variable, even the above analysis only focuses on the integer values of A_{iso}.

Fig. 6 further demonstrates the numerical range of the effective Young's modulus(E_x^H) of VSVT structures with different design configurations (A_{iso}). These modulus variations for VSVT RVEs are compared to the variational bounds for effective moduli of composite materials, such as the Hashin–Shtrikman bound and the Voigt upper limit. It can be seen that as A_{iso} increases, the VSVT design method can generate high-stiffness metamaterial RVE units for porous materials. The Young's modulus of these VSVT RVE units typically exceeds the Hashin–Shtrikman upper bound $E^H = \rho/(3 - 2\rho)$, while gradually approaching the Voigt limit $E^H = \rho$ [21,37].

As the VSVT structure with $A_{iso} = 3$ exceeds the Hashin–Shtrikman upper bound, we can claim that the designed VSVT structures with $A_{iso} = 1 \sim 3$ exhibits sufficient advanced stiffness property over the most common isotropic porous materials in nature. In fact, as A_{iso} significantly increases towards the positive infinity, the VSVT geometry tend to transform into a typical 'horizontal parallel strip pattern' rather than a 'regular porous topology' in the 2D plane, as illustrated by the cases of $A_{iso} = 15, 20$ in Fig. 6. This maximizes stiffness along the x-direction while providing almost no support in the y-direction. Consequently, the corresponding modulus of the RVE will ultimately reach the upper Voigt limit of strength [20,38]. These results imply the potential to achieve excellent axial strength by designing VSVT structures with tunable anisotropy.

However, it should also be noted that merely increasing A_{iso} is not always an effective means to infinitely improve overall compliance performance due to the 'Voigt bound' strength. Fig. 6 clearly indicates that the rate of increase in E_x^H rapidly diminishes as A_{iso} increases. In summary, due to reliability considerations such as multi-directional loading capability, the 3D printing contact angle [39], and smooth connectivity, we believe that an upper limit of $A_{iso} = 3$ is both reasonable and advantageous for constructing VSVT structures for practical applications.

Finally, the elasticity terms of VSVT structures D_{ij}, varying with respect to the relative density ρ, are predicted by the DFN and plotted in Fig. 7. The DFN is set up with a two-hidden-layer structure, and the training time is less than 5 s. In Appendix B, an explicit polynomial fitting function is provided and the corresponding coefficients are given in Table B.1. To avoid complete solid RVE in the optimization process, we reduce the upper bound of ρ from 1 to 0.8 and simultaneously delete out-of-range data in the training process. In overview, these results further approve the above discussions presented in this section. Due to the orthotropic mechanical properties (as $\alpha = 0$), the terms D_{13}, D_{23} are almost equal to 0, while D_{11}, D_{22} present huge difference. Additionally, a new curve for $A_{iso} = 1.5$ is added to the figure to represent an intermediate value, considering the large gap in mechanical properties between $A_{iso} = 1$ and $A_{iso} = 2$.

2.4. Multi-scale porous materials optimization with VSVT

Structural optimization provides an efficient method for imitating the characteristics of natural materials. In this section, a two-step multi-scale optimization method is developed to design VSVT structures. The optimization objective is to achieve the maximum stiffness for VSVT structures. The basic design domain is firstly divided into a number of homogenized quadratic macro-elements. For each macro-element, three design parameters, namely A_{iso}, ρ, and α, are assigned, and its elasticity tensor is determined using an implicit function $D^H(A_{iso}, \rho, \alpha)$. In the first-step, a parametric optimization is performed on the macro-scale FE model with
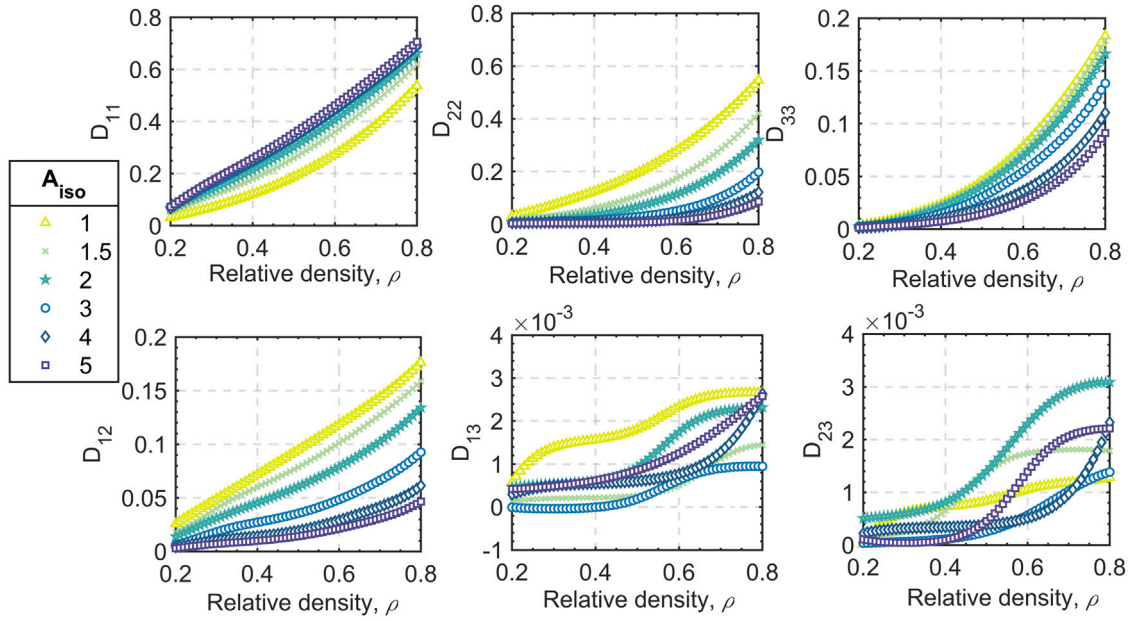
Fig. 7. The matching relationship of homogenized elasticity tensor with respect to relative density ρ. The subscript of D_{ij} corresponds ith row, jth column term of D^H.

homogenized elements to determine a set of optimal design parameters, A_{iso}, ρ, and α, in line with the optimization objectives. Subsequently, the optimal solutions obtained from the first-step procedure are transferred into actual VSVT architectures at the micro-scale through a de-homogenization process.

Theoretically, the design parameters in $D^H(A_{iso}, \rho, \alpha)$ are all continuous variables. However, from Fig. 7, we can see that the stiffness terms (D_{ij}) given by a series of discrete values of A_{iso} can cover the majority of the design domain. Therefore, only a few discrete values for $A_{iso} = 1, 1.5$ (or 2), 3 are used for the structural topology optimization in this work. VSVT structures with different discrete values of A_{iso} can be considered as distinct types of structural components (materials). This allows us to perform a corresponding multi-component topology optimization, analogous to the 'multi-material' design in [40]. The stiffness terms $D^H(A_{iso}, \rho, \alpha)$ varying with respect to the continuous variable A_{iso} are presented in Fig. B.1, which further demonstrates the feasibility of applying discrete values of A_{iso} in the design of VSVT micro-architectures. In this work, we introduce a new design variable, namely the anisotropy index $\mathbf{Z}$, which is a continuous design variable yet only represents a few discrete anisotropic states for VSVT structures, to replace A_{iso} in the optimization process. This is a similar technology of void-solid formations using 0 or 1 densities in SIMP method [23]. In this way, a typical compliance optimization process for the design of VSVT structures can be stated as,

$$
\begin{aligned}
& \text{find} \quad \mathbf{Z}, \boldsymbol{\rho}, \boldsymbol{\alpha} \\
& \min_{\mathbf{Z}, \boldsymbol{\rho}, \boldsymbol{\alpha}} \quad C = \mathbf{F}^T \mathbf{U} \\
& \text{s.t.} \quad V(\mathbf{Z}, \boldsymbol{\rho}) = \frac{\sum_\Omega v_l}{N^e} = \frac{\sum_{l=1}^{N^e} \sum_{i=1}^{m} z_{li} \rho_l}{N^e} \leq V_{frac} \\
& \qquad \mathbf{K}(\mathbf{Z}, \boldsymbol{\rho}, \boldsymbol{\alpha}) \mathbf{U}(\mathbf{Z}, \boldsymbol{\rho}, \boldsymbol{\alpha}) = \mathbf{F}
\end{aligned}
\tag{7}
$$

In Eq. (7), the objective function C in the optimization process is the compliance of the whole structure under an external loading vector $\mathbf{F}$. V is the volume fraction of the total VSVT material over the entire design domain, constrained by an upper bound threshold V_{frac}. Global stiffness matrix $\mathbf{K}$ and nodal displacement vector $\mathbf{U}$ are expressed as the functions of three sets of design variables, $\mathbf{Z}$, $\boldsymbol{\rho}$, $\boldsymbol{\alpha}$. As introduced above, $\mathbf{Z}$ is the anisotropy index, defined by a matrix as $\mathbf{Z} = [z_{li}]_{N^e \times m}$. For its subscripts in element z_{li}, the row index $l = 1, \ldots, N^e$ denotes the lth macro-element in the discretized design domain Ω, and N^e is the total number of macro-elements. The column subscript $i = 1, \ldots, m$ indicates the ith candidate heterogeneous VSVT architecture (a VSVT component), and m is the total number of VSVT candidate components expected to used in the optimization process. Therefore, the value of $z_{li} \in [0, 1]$ represents the presence percentage of ith candidate heterogeneous VSVT component at lth macro-element. Each element ρ_l in the relative density design vector $\boldsymbol{\rho} = [\rho_l]_{l=1}^{N^e}$ represents the local solid volume fraction of VSVT materials in the lth macro-element, and $\rho_l \in [0, 1]$. The design variable α_l in the vector $\boldsymbol{\alpha} = [\alpha_l]_{l=1}^{N^e}$ represents the rotation angle of the principal direction of the VSVT component at the lth macro-element with respect to the positive x axis, and $\alpha \in (-\pi/2, \pi/2)$. The terms $v_{li} = z_{li} \cdot \rho_l$ is the actual volume fraction of ith candidate VSVT structure at lth element.

It is evident that the mixing status of m types of VSVT structures in the lth macro-element can be fully described by the row vector $\{\mathbf{z}_i\}_l$. Taking into account the challenges of the de-homogenization process, different VSVT components are not allowed to mix within a single macro-element in this work. Consequently, after optimization, the element should either be completely empty or contain only one candidate VSVT component. As a result, the convergent $\{\mathbf{z}_i\}_l$ should remain in the form specified by Eq. (8), in which a non-zero value of $z_{li} = 1$ indicates the ith anisotropic VSVT component in the lth element.

$$\{\mathbf{z}_i\}_l = \begin{cases} \mathbf{0}, & \text{No solid material in } l\text{th element} \\ \\ \{z_{li} = 1, z_{lj} = 0\}, & \text{where } j = 1, 2 \ldots m \,\&\, j \neq i \end{cases} \tag{8}$$

To enforce well-posedness and avoid 'checkboard' phenomenon in the macro-scale optimization process [5,41], a 'density filter' technique is applied on the anisotropy index $\mathbf{Z}$, relative density ρ, and principal direction $\boldsymbol{\alpha}$. Take the anisotropy index $\mathbf{Z}$ as an example,

$$\begin{cases} \tilde{\mathbf{Z}} = \mathbf{PZ} \\ P_{ij} = \frac{h_{ij}}{\sum_{k=1}^{N^e} h_{ik}}, & h_{ij} = \max(R - \|x_i - x_j\|_2, 0) \end{cases} \tag{9}$$

where P_{ij} is a term of the regularization mapping matrix $\mathbf{P}$. Matrix $\tilde{\mathbf{Z}}$ represents the anisotropy index field after density filtering processing. $\|x_i - x_j\|_2$ is the Euclidean norm between the centers of ith and jth elements, R is the filter radius.

Subsequently, a Heaviside projection is utilized to process $\tilde{\mathbf{Z}}$ to further increase the topology optimization quality in the vicinity of structural boundary by penalizing the intermediate values of z_{li} between 0, 1 with a filter scheme. The penalized elemental anisotropy field $\bar{\mathbf{Z}}$ is obtained using the Heaviside projection method [42] as,

$$\bar{z}_{li} = H(\tilde{z}_{li}) = \frac{\tanh(\beta\eta) + \tanh(\beta(\tilde{z}_{li} - \eta))}{\tanh(\beta\eta) + \tanh(\beta(1 - \eta))} \tag{10}$$

where β and η are the 'threshold' and 'sharpness' parameters of the Heaviside projection, respectively.

As discussed above, $z_{li} = 1$ or 0 implies the presence or absence of a VSVT structure with the ith anisotropy index (A_{iso}) at the lth macro-element. Intermediate values of z_{li} within the range $[0, 1]$, which would indicate a mixture of different VSVT components, are not considered in this work. Therefore, a modified field $\mathbf{W} = \{w_{l1}, w_{l2}, \ldots, w_{lm}\}_{l=1}^{N^e}$ is defined through a SIMP penalizing process based on the projection variable field $\bar{\mathbf{Z}} = \{\bar{z}_{l1}, \bar{z}_{l2}, \ldots, \bar{z}_{lm}\}_{l=1}^{N^e}$, to further penalize intermediate values of $\mathbf{Z}$. Each term in the matrix $\mathbf{W}$ is defined as $w_{li} = \bar{z}_{li}^p$ with a penalty factor $p > 1$. This ensures that $\mathbf{W}$ provides precise, well-posed topological information in the multiscale optimization and subsequent de-homogenization processes.

In Eq. (7), the global stiffness matrix $\mathbf{K}$, is assembled from the element stiffness matrices $\mathbf{Ke}^l$ as:

$$\mathbf{K} = \sum_{l=1}^{N^e} \mathbf{Ke}^l = \sum_{l=1}^{N^e} \left(\int_{\Omega_l} \mathbf{B}_j^T \mathbf{D}_l(\mathbf{Z}_l, \rho_l, \alpha_l) \mathbf{B}_k \, d\mathbf{x} \right), \tag{11}$$

where $\mathbf{B}$ is the strain–displacement matrix of the shape function derivatives, $\mathbf{D}_l$ is the elasticity tensor of element l. Considering an element with different VSVT candidate components, its $\mathbf{D}_l$ can be expressed via the following interpolation function, which is analogous to the ones in multi-material topology method as in [43],

$$\mathbf{D}_l = \sum_{i=1}^{m} w_{li} \prod_{\substack{j=1 \\ j \neq i}}^{m} (1 - \gamma w_{lj}) \mathbf{M}(\alpha_l) \mathbf{D}_i^H(\rho_l) \mathbf{M}^T(\alpha_l), \qquad l = 1, \ldots, N^e. \tag{12}$$

Eq. (12) penalizes mixing between candidate VSVT components (materials) through mixing parameter $\gamma \in [0, 1]$[5]. $\mathbf{D}_i^H(\rho_l)$ is the homogenized elasticity tensor of a candidate VSVT structure with ith anisotropic index in element l, whose internal terms $(\mathbf{D}_i^H)_{jk}$ are expressed as a fitting function $(\mathcal{F}_i(\rho_l))_{jk}$ as shown in Fig. 7. $\mathbf{M}$ is a standard tensor transformation matrix for adjusting material orientation, as defined in Eq. (20).

The optimization problem can be solved by a typical iterative gradient based algorithm, e.g., the 'Method of Moving Asymptotes' (MMA) algorithm. As the objective function f is the structural compliance C, the derivatives of the compliance C with respect to each design variable are given by,

$$\frac{\partial f}{\partial \mathbf{z}_i} = \frac{\partial \tilde{\mathbf{z}}_i}{\partial \mathbf{z}_i} \frac{\partial \bar{\mathbf{z}}_i}{\partial \tilde{\mathbf{z}}_i} \frac{\partial \mathbf{w}_i}{\partial \bar{\mathbf{z}}_i} \frac{\partial f}{\partial \mathbf{w}_i} \tag{13}$$

$$\frac{\partial f}{\partial w_{li}} = -\mathbf{U}^T \frac{\partial \mathbf{K}}{\partial w_{li}} \mathbf{U} = -\mathbf{U}^T \frac{\partial \sum_1^{N^e} \mathbf{Ke}^l}{\partial w_{li}} \mathbf{U} \tag{14}$$

$$\frac{\partial f}{\partial \rho_l} = -\mathbf{U}^T \frac{\partial \mathbf{K}}{\partial \rho_l} \mathbf{U} = -\mathbf{U}^T \frac{\partial \sum_1^{N^e} \mathbf{Ke}^l}{\partial \rho_l} \mathbf{U} \tag{15}$$

$$\frac{\partial f}{\partial \alpha_l} = -\mathbf{U}^T \frac{\partial \mathbf{K}}{\partial \alpha_l} \mathbf{U} = -\mathbf{U}^T \frac{\partial \sum_1^{N^e} \mathbf{Ke}^l}{\partial \alpha_l} \mathbf{U} \tag{16}$$

Considering Eqs. (9) and (10), the terms in Eq. (13) can be further simplified as,

$$\left[\frac{\partial \bar{\mathbf{z}}_i}{\partial \mathbf{z}_i}\right] = \mathbf{P}^T$$

$$\left[\frac{\partial \tilde{\mathbf{z}}_i}{\partial \bar{\mathbf{z}}_i}\right] = \frac{\partial \tilde{\mathbf{z}}_{kj}}{\partial \bar{\mathbf{z}}_{li}} = \begin{cases} \frac{\beta(1-\tanh^2(\beta(\bar{z}_{li}-\eta)))}{\tanh(\beta\eta)+\tanh(\beta(1-\eta))}, & \text{if } l=k \text{ and } j=1 \\ 0, & \text{otherwise} \end{cases}$$

$$\left[\frac{\partial \mathbf{w}_i}{\partial \bar{\mathbf{z}}_i}\right] = \frac{\partial \mathbf{w}_{kj}}{\partial \bar{\mathbf{z}}_{li}} = \begin{cases} p\bar{z}_{li}^{p-1}, & \text{if } l=k \text{ and } j=1 \\ 0, & \text{otherwise} \end{cases} \tag{17}$$

For the derivatives of the local stiffness matrix with respect to $\mathbf{W}$, it can be expressed with a standard FEM model as,

$$\frac{\partial \sum_1^{N^e} \mathbf{K}\mathbf{e}^l}{\partial w_{li}} = \int_{\Omega_l} \mathbf{B}'_e \frac{\partial \mathbf{D}_k}{w_{li}} \mathbf{B}_e dx dy. \tag{18}$$

(x, y) and $\mathbf{B}_e$ are the coordinates and strain–displacement matrix over the domain of element l. The inner terms are stated as,

$$\frac{\partial \mathbf{D}_k}{w_{li}} = \begin{cases} \prod_{\substack{j=1 \\ j\neq i}}^{m}(1-\gamma w_{lj})[\mathbf{D}_{li}^H]^\alpha - \sum_{\substack{p=1 \\ p\neq i}}^{m} \gamma w_{lp} \prod_{\substack{r=1 \\ r\neq i \\ r\neq p}}^{m}(1-\gamma w_{lr})[\mathbf{D}_{lp}^H]^\alpha, & \text{if } l=k \\ 0, & \text{otherwise} \end{cases} \tag{19}$$

where $[\mathbf{D}_{ki}^H]^\alpha$ is the simplified notation of elasticity tensor omitting the Rotation matrix terms, and given by,

$$[\mathbf{D}_{li}^H]^\alpha = \mathbf{M}(\alpha_l)\mathbf{D}_i^H(\rho_l)\mathbf{M}^T(\alpha_l)$$

$$\mathbf{M}(\alpha_l) = \begin{bmatrix} \cos^2(\alpha_l) & \sin^2(\alpha_l) & -2\cos(\alpha_l)\sin(\alpha_l) \\ \sin^2(\alpha_l) & \cos^2(\alpha_l) & 2\cos(\alpha_l)\sin(\alpha_l) \\ \cos(\alpha_l)\sin(\alpha_l) & -\cos(\alpha_l)\sin(\alpha_l) & \cos(2\alpha_l) \end{bmatrix} \tag{20}$$

Similarly, Eqs. (15) and (16) can be expressed as,

$$\frac{\partial \mathbf{D}_k}{\partial \rho_l} = \sum_{i=1}^{m} w_{li} \prod_{\substack{j=1 \\ j\neq i}}^{m}(1-\gamma w_{lj})\frac{\partial[\mathbf{D}_{ki}^H]^\alpha}{\partial \rho_l},$$

$$\frac{\partial[\mathbf{D}_{ki}^H]^\alpha}{\partial \rho_l} = \mathbf{M}(\alpha_k)\frac{\partial \mathbf{D}_i^H(\rho_k)}{\partial \rho_l}\mathbf{M}(\alpha_k)^T$$

$$\frac{\partial(\mathbf{D}_i^H(\rho_k))_{pq}}{\partial \rho_l} = \begin{cases} \frac{\partial(F_i)_{pq}}{\partial \rho_l}, & \text{if } l=k \\ 0, & \text{otherwise} \end{cases} \quad \text{term index } pq = 11, 12, \ldots, 33 \text{ for } \mathbf{D}_i^H \tag{21}$$

and

$$\frac{\partial[\mathbf{D}_{ki}^H]^\alpha}{\partial \alpha_l} = \begin{cases} \frac{\partial \mathbf{M}(\alpha_k)}{\alpha_l}\mathbf{D}_i^H M(\alpha_k)^T + M(\alpha_k)\mathbf{D}_i^H \frac{\partial \mathbf{M}^T(\alpha_k)}{\alpha_l}, & \text{if } l=k \\ 0, & \text{otherwise} \end{cases} \tag{22}$$

For the global volume constraint and its corresponding derivative functions in Eq. (7), given by,

$$g = \frac{\sum v_{li}}{N^e} - V_{frac} = \frac{\sum \bar{z}_{li}\rho_l}{N^e} - V_{frac}, \qquad l=1\ldots N^e, i=1, \ldots, m$$

$$\frac{\partial g}{\partial \mathbf{z}_i} = \frac{\partial \bar{\mathbf{z}}_i}{\partial \mathbf{z}_i}\frac{\partial \tilde{\mathbf{z}}_i}{\partial \bar{\mathbf{z}}_i}\frac{\partial g}{\partial \tilde{\mathbf{z}}_i} = \frac{\partial \bar{\mathbf{z}}_i}{\partial \mathbf{z}_i}\frac{\partial \tilde{\mathbf{z}}_i}{\partial \bar{\mathbf{z}}_i}\frac{\rho_l}{N^e} \tag{23}$$

$$\frac{\partial g}{\partial \rho_l} = \sum_{i=1}^{m}\frac{\bar{z}_{li}}{N^e}, \qquad \frac{\partial g}{\partial \alpha_l} = 0$$

where its terms are identical to those in Eqs. (7) and (17). For the sake of clarity, we simplified the density filter expression of design variables ρ and α as in Eqs. (20) to (23). Similar with Eq. (9), these design variables should all be substituted by $\bar{\rho} = \mathbf{P} \cdot \rho$ and $\bar{\alpha} = \mathbf{P} \cdot \alpha$ in the practical program implementation.

To avoid undesirable local optima, five continuation steps with the material interpolation parameters, i.e., $p = [1, 2, 3, 3, 3]$ and $\gamma = [0, 0.25, 0.5, 0.75, 1]$ are performed in the optimization process. Each continuation step is considered to have converged after reaching the maximum number of iterations, as defined the maximum of iterations 'MaxIter' = [50, 50, 50, 50, 200], or when the variable change is less than the convergence tolerance tol = 0.01. To avoid the 'gradient vanishing' problem, the sharpness parameter β for Heaviside projection is kept as 1 in early stages of the optimization process. After the convergence of p and γ in the
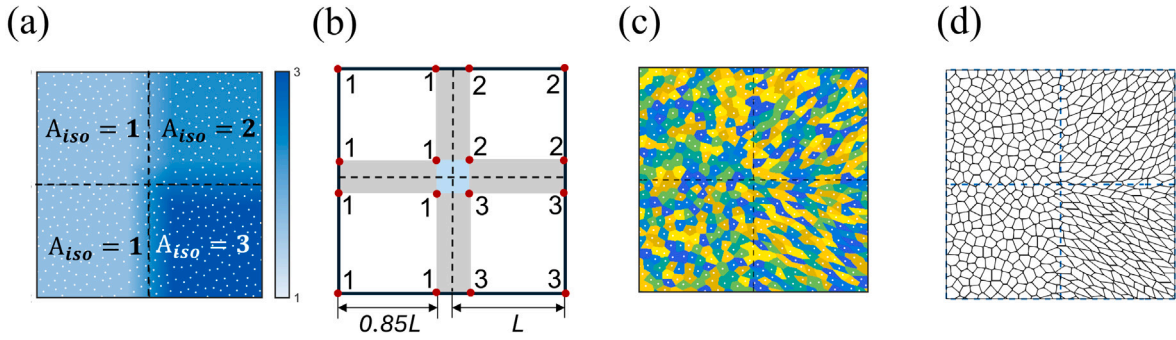
Fig. 8. The demonstration for the natural connectivity of VSVT porous structures. (a) The anisotropy ratio field of four RVE elements, with initial '$A_{iso} = 1, 2, 3$'. The white dots denote the Voronoi seeds of the VSVT structure. (b) The detailed linear-interpolation meshgrid for anisotropy ratio field. (c) The VSVT structure generated using the updated anisotropy ratio field. Different color blocks represent individual Voronoi cells. (d) The final VSVT structure with smooth connectivity in the design domain that the original RVE boundaries, denoted by the dashed lines, are almost unrecognizable by the naked eye.

last continuation step, β is increased by 1 every 5 iterations until it reaches a maximum value of 25. Additionally, the Heaviside threshold parameter η is kept at 0.5 throughout the entire optimization process. To avoid local minimum problems commonly encountered in angle optimization, we run 20 extra sub-iterations solely for optimizing α every 30 main iterations. Although the penalty factor p in Eq. (17) and the interpolation coefficient γ in Eq. (19) can penalize material mixing, slight mixing may still occur at interfaces among different VSVT candidate components in the optimal solutions, especially when density filter matrix **P** uses a big filter radius. For these cases, we adopt an extra post-processing step, as referenced in [43], to achieve sharp boundaries. For detailed information on the algorithm and post-processing code, please refer to Appendix C.

2.5. De-homogenization and connectivity

After obtaining the optimal design solution for each macro-element, the corresponding VSVT architecture is determined through a de-homogenization process based on the target design parameters, A_{iso} (**Z**), ρ and α. Firstly, the relative density ρ of each macro-element is converted into the number of Voronoi seeds N_s and truss thickness t by solving the $\rho(N_s, t)$ function using MATLAB's 'fmincon' function. Subsequently, a varied-shape Voronoi tessellated (VSVT) wireframe over the entire design domain is generated within a single step based on the optimal design parameters of each macro-element, i.e., the number of Voronoi seeds N_s, anisotropy index A_{iso} and material principal direction α. Finally, the VSVT wireframe is further reinforced according to the thickness information t.

It had been widely recognized that the 'connectivity' between adjacent elements is a crucial issue in the design of multiscale materials and structures. Since VSVT uses a 'seeding' based technology to construct multiscale lattice structures, the Voronoi tessellation is only performed once on the entire design domain in a single step, rather than on individual elements during the de-homogenization process. Consequently, the VSVT design method is capable to generate a relatively smooth and natural material connection, automatically, between neighboring macro-elements [23], without the need of the predefined 'fixed boundary material interfaces', as used in many other works [26,27,44].

On the other hand, one of the main aims of this proposed VSVT method is to enable the design of multiscale materials and structures with tunable anisotropy. The advantages of the nature connectivity provided by the VSVT method remain valid in theory even when highly anisotropic elements are considered. However, from a view of practical manufacturability, it is better to introduce an additional operation to ensure smooth, gradual transitions of the anisotropic Voronoi lattice shapes between macro-elements. An example, shown in Fig. 8, illustrates both the advantageous connectivity and the smoothing operation of a VSVT structure, in which each macro-element possesses distinct different anistropy ratios, namely A_{iso}. Fig. 8(a) shows a VSVT design domain containing four macro-elements, each with different anisotropy ratios as, $A_{iso} = 1, 1, 2, 3$. The Voronoi seeds are marked as white dots in the image. To ensure smooth transitions of anisotropic Voronoi lattice shapes between the boundaries of macro-elements, a linear interpolation operation is applied to the anisotropy ratio field A_{iso}. Fig. 8(b) illustrates the boundary regions where the anisotropy ratios of the Voronoi seeds are adjusted to intermediate values through this linear interpolation operation. Those regions are divided into three different types, indicated by white, grey and blue colors in Fig. 8(b). In the white region, the anisotropy ratios of the Voronoi seeds remain unchanged. In contrast, the anisotropy ratios in the grey and blue regions are adjusted to intermediate values between the initial A_{iso} values of two or four macro-elements, respectively. With the updated anisotropy ratios A_{iso} for Voronoi seeds in the boundary regions, the VSVT structure across the entire design domain is generated using Eq. (3), as illustrated in Fig. 8(c). The final VSVT wireframe model, abstracted from Fig. 8(c), is shown in Fig. 8(d). After removing the color marks, no obvious dividing lines are observed in the design domain, which demonstrates the VSVT's capability in designing multiscale materials with natural material-like connectivity. In summary, the final VSVT design embodies the 'stochastic', 'anisotropic', and 'multi-scale' characteristics mentioned in the introduction. Additionally, the corresponding micro-porous cells exhibit disorder, non-uniformity, and aperiodicity.
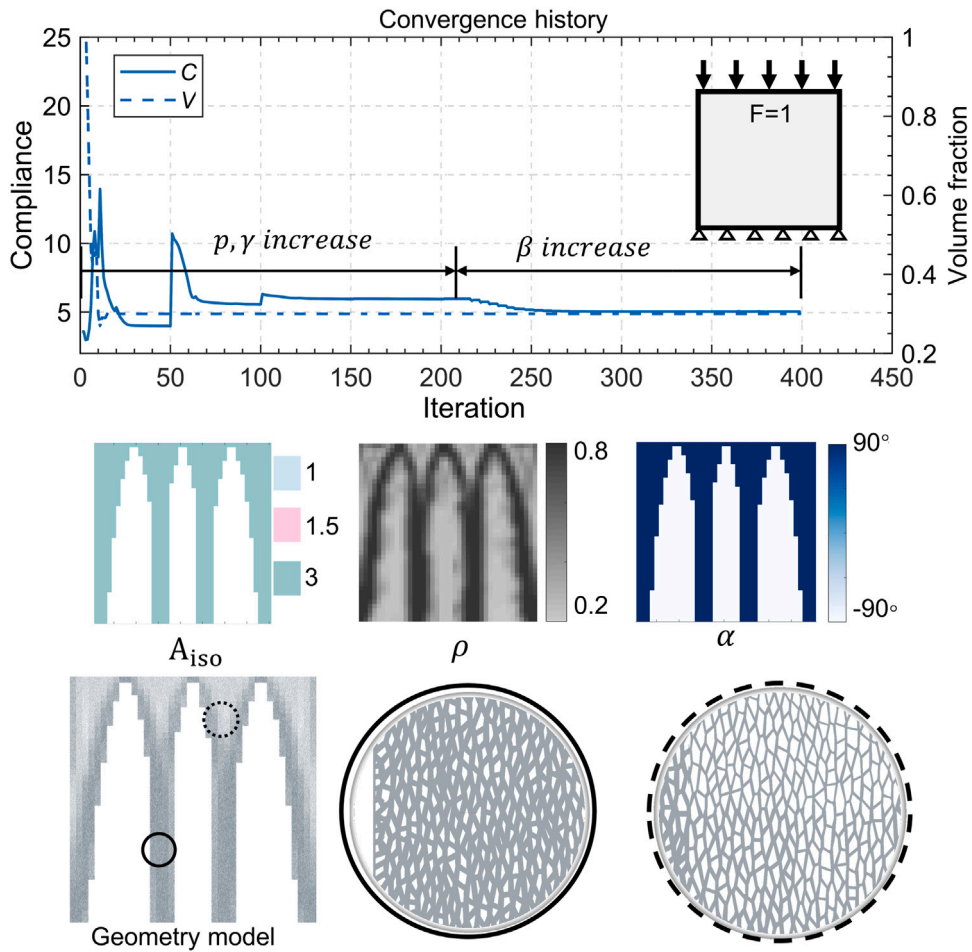
Fig. 9. The optimal VSVT porous structure for the unidirectional compression case. Different stages of the optimization step are noted in the convergence history. The boundary condition and final solution of A_{iso}, ρ and α are shown as captures. For this case, the VSVT materials are all optimized to $A_{iso} = 3$ configuration due to specific loading condition.

3. Numerical examples

3.1. Uni-directional compression example

A typical and simple 'uni-directional loading' example is demonstrated here to verify the effectiveness of VSVT structures with tunable anisotropy in topology optimization. A 80 mm × 80 mm design domain is discretized into a 40 × 40 meshgrid layout for the 'minimum compliance performance' objective. An external force $F = 1$ N is uniformly distributed along the domain's upper edge, while the boundary edges are fixed in all degrees of freedom, as depicted in Fig. 9. The normalized Young's modulus, Poisson's ratio and volume fraction constraint are set as $E_s = 1$ MPa, $\nu = 0.3$ and $V_{frac} = 0.3$, respectively.

Regarding the anisotropy index **Z**, we choose $m = 3$, namely that three values of $A_{iso} = 1, 1.5, 3$ are used for the candidate VSVT structures in this example. The use of VSVT structures with $A_{iso} = 1.5$ instead of $A_{iso} = 2$ can avoid the significant jump in mechanical properties between the VSVT structures with $A_{iso} = 1$ and $A_{iso} = 2$. For VSVT structures with $A_{iso} = 3$, its stiffness along x-direction is approximately the same as that of VSVT structures with $A_{iso} = 4$ or 5, but the stiffness along the y-direction is significantly higher. For the $A_{iso} > 5$ VSVT structure, their corresponding topology is relatively closer to strip struts rather than to closed-cell pores, and are therefore not considered in this work. In view of above considerations, we believe that the VSVT structures with $A_{iso} = 1, 1.5, 3$ will cover the majority of the design space and achieve superior design performance through the optimization process.

According to the principle of mechanics, the principal stress field of this 'uni-directional loading' problem, given in Fig. 9, is oriented along the vertical direction. Therefore, it is expected that the optimal design of the lattice structures for this problem should predominantly contain anisotropic elements, with their moduli aligned with the vertical direction. The convergence curves of the optimization process and the final optimal solutions in terms of A_{iso}, ρ, α are presented in Fig. 9. The compliance ultimately decreases to 5.05, and the volume fraction precisely converges to 0.3, as specified by the constraint. Consistent with the prediction
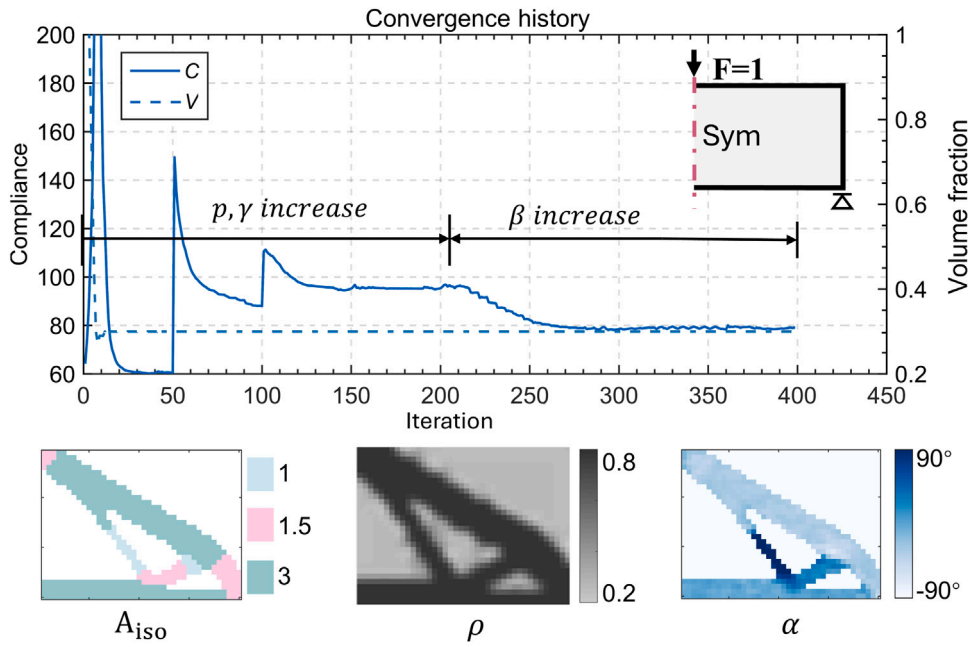
Fig. 10. The VSVT optima of MBB case by topology optimization. The boundary condition and final solution of A_{iso}, ρ and α are illustrated as captures under the convergence history.

from the principle of mechanics, the final design for this problem is predominantly occupied with VSVT units with $A_{iso} = 3$, while no units with $A_{iso} = 1$ or 1.5 are present. The material principal direction α of each VSVT unit is $90°$, which ensures that the principal modulus direction of the optimal structure aligns with the vertical direction. Furthermore, in this optimal VSVT configuration, the corresponding de-homogenized geometry model closely resembles the optimal topology obtained by the SIMP method, in which the majority of material gathers around the top edge and forms a 'tree branch' pattern [45].

3.2. MBB example

In this section, the VSVT method is applied to design an MBB beam. A 40×30 grid mesh is used to discretize the 160 mm $\times$ 120 mm design domain. Given that the strength-to-volume ratio is a key focus in porous material design, we aim to optimize the compliance performance of the VSVT structure. The relative density threshold (porosity threshold) remains consistent with Section 3.1, specifically $0.2 \leq \rho \leq 0.8$, with a global volume fraction of $V_{frac} = 0.3$.

The optimization process for this MBB beam example is illustrated in Fig. 10, which shows that the compliance value has converged to 78.7. The final optimal solution in terms of the design variables A_{iso}, ρ, and α is depicted below the convergence curve. From the relative density ρ distribution, as shown in Fig. 10, we observe that the material is concentrated into a narrow path to support the external force, as indicated by the black shadow region in the image. In the main slender areas, i.e., the diagonal and bottom horizontal rods, the local maximum principal stress aligns with the direction of the material-concentrated path and is significantly higher than the stress component in other directions. As a result, the local strain field approximates a uni-directional compressive or tensile status. In view of this, these regions are assigned materials with high anisotropic properties ($A_{iso} = 3$) by the optimization process, with the principal material direction parallel to the path direction at $-36.5°$ or $0°$, as shown in Fig. 10. These features contribute to increased structural stiffness. On the other hand, local regions at top-left corner, bottom-right corner and the most part of the inner short slender, as shown in the A_{iso} image of Fig. 10, are assigned VSVT materials (components) with low anisotropic ratios ($A_{iso} = 1$ or 1.5). This is because the principal stress directions in these locations vary significantly and rapidly across the their neighboring areas. The VSVT structures (components) with low anisotropic ratios possess relatively isotropic property, thereby providing enhanced load carrying capacity from various directions for those regions. In summary, this MBB example demonstrates that the proposed VSVT approach offers tunable anisotropy design flexibility, enabling the optimization of structural performance under complex loading conditions.

3.3. Design flexibility from de-homogenization

The optimal multiscale porous structure for this MBB example is obtained using a de-homogenization process and is shown in Fig. 11(a). As expected, the Voronoi cells in different macro-elements exhibit distinct relative density and anisotropy ratios. Furthermore, as discussed in Section 2.2, when the seed amount N_s is within the designed range, a VSVT RVE unit demonstrates
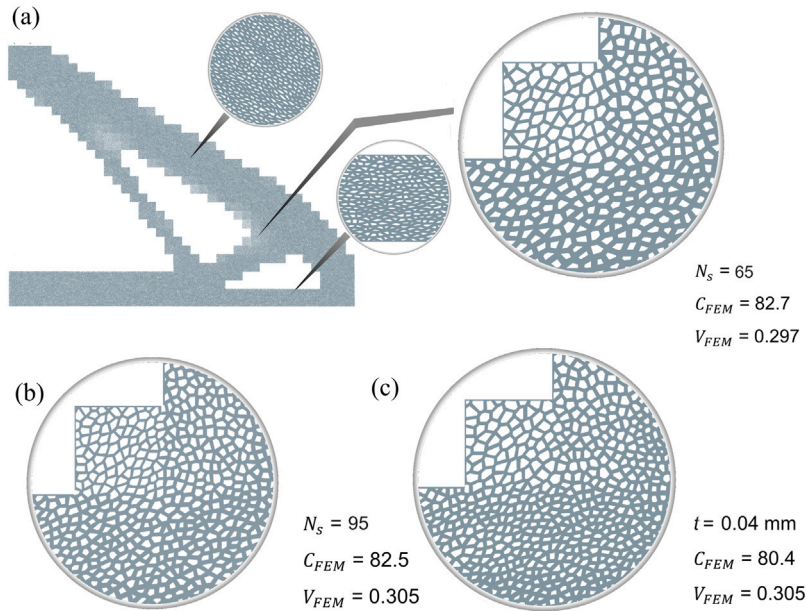
Fig. 11. The detailed VSVT porous structure for the MBB case by de-homogenization process. (a) present an overview of the whole VSVT structure in domain, while its three captures present several typical elements in isotropic or anisotropic mode. The alignment of truss in capture varied identical to the stress direction. (a), (b), (c) compared different VSVT model with respect to de-homogenized rules as 'same N_s = 65','same N_s = 95' and 'same t = 0.16mm' for elements among the design domain. Notably, t indicates the true thickness of trusses rather than the normalized value. The compliance value and volume fraction of the corresponding model are computed using ABAQUS FE model and are also noted in the images.

strong statistical stability in its mechanical properties. Therefore, the same optimal solution for a particular problem can be de-homogenized into many different VSVT architectures, which possess almost the same mechanical performance yet have distinct microscale configurations. This feature allows us to perform the optimization design with additional or multidisciplinary objectives.

In Fig. 11, another two different topological architectures as shown in (b) and (c) that have almost the same optimal mechanical performance as (a) are demonstrated. Since the macroscale views are all similar, we only plot the configurations for (b) and (c) that are in the same region as Fig. 11(a). The de-homogenization rules for the cases shown in Fig. 11(a), (b), and (c) are presented as follows, 'VSVT elements with N_s = 65', 'VSVT elements with N_s = 95' and 'VSVT elements with t = 0.16 mm, respectively. The corresponding compliance and volume fraction computed by the detailed FEM model are also presented in Fig. 11, as C_{FEM} and V_{FEM}. These results show discrepancies of less than 5% compared to those obtained using the standard TO (SIMP) method, which further confirms the high accuracy of our homogenization process for the VSVT structures, as discussed in Section 2.2. Since all configurations achieve very similar FE results, with differences within 2.8%, it is evident that the geometrical stochasticity of the VSVT material, generated by Poisson Disk Sampling method in Section 2.1 or through the additional connectivity processing in Section 2.5, has almost negligible influence on the compliance. This highlights the numerical stability of the proposed VSVT approach. For more detailed information regarding the FEM model and the computation process, please refer to Appendix C.

In practical applications, the design flexibility offered by the VSVT method can be utilized to develop additional functionalities or physical properties while maintaining optimal mechanical performance. For many industrial manufacturing processes, such as those involving battery reactors or heat exchangers, this flexibility enables adjustable reaction efficiency due to the tailorable Specific Surface Area (SSA). Similarly, in clinical applications, the VSVT method allows for the customization of porous femoral implants, ensuring a specific range of pore amounts N_s to promote quick vessel growth and nutrient transmission in vivo [46]. Additionally, varying the truss thickness t enables VSVT structures to tune local stress distribution under body loading [47], which can be used to eliminate stress shielding problems for bone implants.

To further illustrate the advantages of design flexibility of the VSVT method, we present a 'mechanical-thermal clock' example, as shown in Fig. 12. This example demonstrates several VSVT structures with similar optimal mechanical performance, such as compliance, while exhibiting distinct adjustable heat dissipation characteristics. This type of metamaterial possesses both high stiffness and the ability to pre-engineer thermal differences, thereby generating thermal stress under specific temperature conditions. These characteristics make them advantageous for applications such as thermoelectric generators, thermal sensors, and heat exchangers [48,49].

The loading and boundary conditions for this example are the same as those in the uni-compression case presented in Section 3.1. The design range of the relative density is $\rho \in [0.2, 0.5]$, and the global volume fraction is set to be 0.5, as depicted in Fig. 12(a). The mesh grid size is modified to be 20×20. After the first step of compliance optimization, the optimal solutions of marco-elements
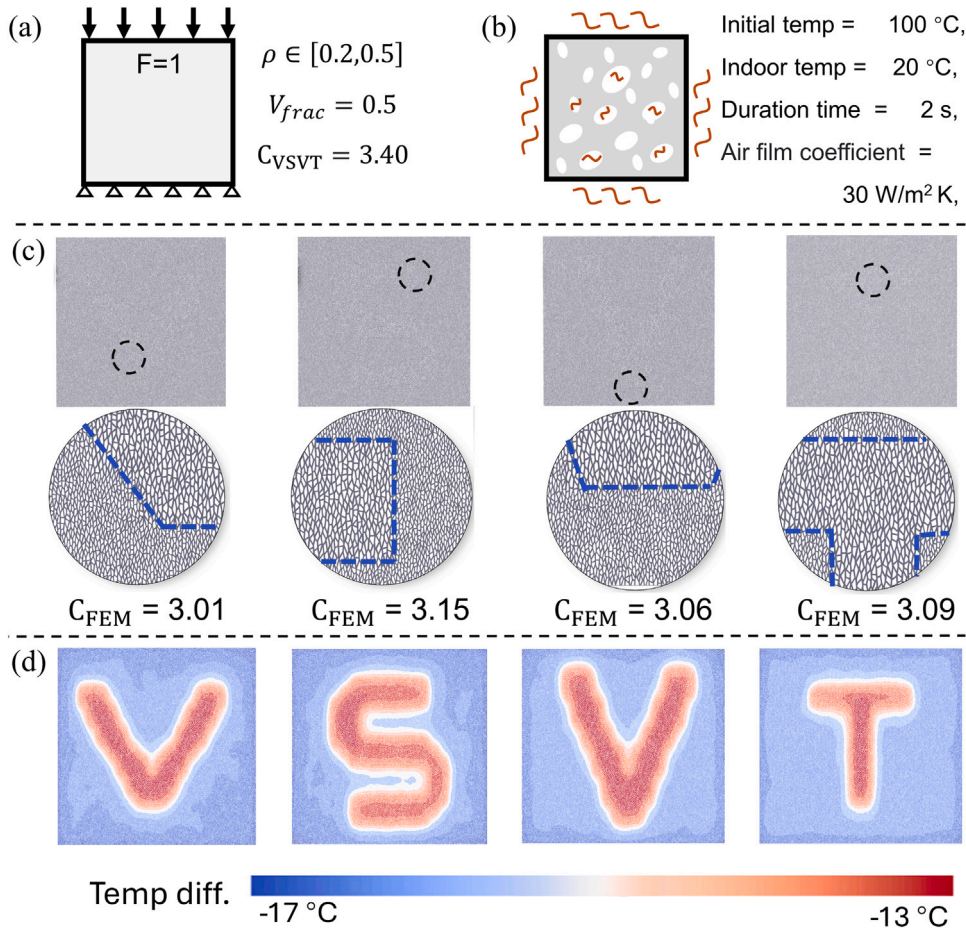
Fig. 12. The VSVT thermal 'mechanical clock' design for Uni-compressive bounding by de-homogenization process. (a) present the loading boundary for compliance optimization. (b) present the boundary setting for Heat dissipation FE model, which simulates typical working environment of electronic component's supporting plate. (c) demonstrate the geometry model and FEM-computed compliance values for four different de-homogenization set-ups. The four cases show similar apparent architecture and compliance, but difference in detail as captures shows. (d) is the temperature distribution of four cases after heat transferring for 2s (in a form of differences in value from initial 100 °C). The tuned elements present a 'VSVT' word-symbol refer to our design. Herein, two 'V' characters are different due to their distinct size and angle in the draft. The simulation is completed by ABAQUS with a material property of middle-carbon steel, i.e. density 7.85×10^3 Kg/m^3, thermal conductivity 43.0 W/m K, specific heat capacity 477 J/kg K.

all converge to $\rho = 0.5, A_{iso} = 3, \alpha = 90°$, which is then de-homogenized into four different plates, as shown in Fig. 12(c). During the de-homogenization process, the truss thickness t of the macro-elements in each plate is decreased by 25% in certain regions, from 0.12 mm to 0.09 mm. The corresponding borders of these regions have been marked as blue dash line in Fig. 12(c) close-ups for identification. This reduction results in a 23.5% decrease in the specific surface area (SSA) of the macro-elements in those regions, leading to reduced heat convection efficiency. Consequently, the temperature difference ratio for the two type elements (the original elements and the elements with reduced SSA) is predictable and almost proportional to the ratio of SSA. This relationship is given by,

$$\frac{\Delta T_{red}}{\Delta T_{blue}} = -13 / -17 = 0.76$$
$$\approx 1 - \frac{\Delta SSA}{SSA} \approx 1 - \frac{\Delta t}{t} = 0.75 \tag{24}$$

To test their thermal performance, all four plates are initially pre-heated to 100°C and subjected to a natural air heat transfer boundary, as shown in Fig. 12(b), simulating a CPU motherboard work environment. Subsequently, the temperature field rapidly decreases towards room temperature, resulting in the four plates clearly displaying the four letters 'V', 'S', 'V', 'T', respectively, as illustrated in Fig. 12(d). This occurs because the lattice structural elements in the regions of these letters possess reduced heat convection efficiency, as explained in above. In summary, while the proposed VSVT structure with an SSA adjusting mechanism is only used for temperature distribution control in this example, it also shows high potential for use as a substrate plate in various biological, chemical, or electrical reactions to achieve a tuned reaction rate.

Table 1
The improvement on compliance performance of the VSVT structure.

Mesh grid	ρ bounds	C_{VSVT} [a]	C_{FEM}	C_{Iso}	C_{IsoFEM}	TO Error[b]	Improvement[c]
48 × 36	0.2–0.8	79.2	75.5	98.0	105.7	4.7%	23.7%
40 × 30	0.2–0.8	78.7	82.8	98.1	106.9	5.2%	24.7%
32 × 24	0.2–0.8	81.7	87.9	97.7	103.6	7.6%	19.6%
48 × 36	0.2–0.5	153.4	155.3	200.3	202.5	1.2%	30.6%
40 × 30	0.2–0.5	150.4	140.1	198.8	206.6	−6.9%	32.2%
32 × 24	0.2–0.5	149.5	138.5	195.8	190.7	−7.3%	31.4%

[a] C_{VSVT} and C_{FEM} are the compliance values computed by TO method and FE model. C_{Iso} and C_{IsoFEM} are the compliance results for the isotropic porous material.
[b] Topology optimization error equals $(C_{FEM} - C_{VSVT})/C_{VSVT}$.
[c] The improvement is calculated as $(C_{Iso} - C_{VSVT})/C_{Iso}$.

Table 2
The comparison of compliance performance between VSVT structure and optimized solid structure.

Cases	VSVT-1	Isotropic porous structure	**Optimized solid structure**	VSVT-2
Relative density	0.2–0.8	0.2–0.8	**0–1**	**0.2–1**
Compliance	78.7	98.1	**65.1**	**56.8**

3.4. The advantages of VSVT structures with tunable anisotropy over isotropic structures

In this section, we further verify the advantages of applying VSVT structures with tunable anisotropy in design. Specifically, we compare the optimal compliance performance of VSVT structures with that of typical isotropic lattice structures. The isotropic designs are obtained by only considering $A_{iso} = 1$ in the above VSVT (multi-component) optimization process.

The optimization results for 'MBB' beams under different meshgrid sizes and relative density bounds ρ are presented in Table 1. This table provides a comparison between the optimal results of anisotropic VSVT structures and isotropic structures, which are also validated through detailed FEM analysis. The optimization results provided by the 40 × 30 meshgrid for this 'MBB' example can be considered convergent solutions, as the compliance values exhibit only 4% to 5% variations when the meshgrid density is decreased 80% (32 × 24) or increased 120% (48 × 36). The average compliance error between the FE and TO models is approximately 6%, as shown in Table 1. Given this minor error, we believe that our numerical homogenization method presented in Section 2.2 is sufficiently accurate. The detailed FE model is illustrated in Appendix D.

It can be seen that the average compliance values of VSVT structures are 20% ∼ 30% lower than those of isotropic porous structures, indicating a significant stiffness improvement as shown in the last column of Table 1. Further, the VSVT structures with anisotropy features show higher relatively stiffness improvement over the isotropic structures when the upper bound of the relative density ρ_{max} changes from 0.8 to 0.5. Refer to Fig. 7, the difference of the principal elasticity (D_{11}) between anisotropic VSVT structures ($A_{iso} = 3$) and isotropic structures ($A_{iso} = 1$) is more pronounced when the relative density ρ decrease from 0.8 to 0.5. In this way, since the relative density will converge to its ρ_{max} for most macro-elements in the final optimal solution, thus a lower ρ_{max} in set-up will finally lead to a larger stiffness improvement for VSVT design.

Furthermore, a more comprehensive comparison between VSVT porous structure and a typical TO optimized solid structure is performed and shown in Table 2. According to the practical requirements of porous structure [5,24], the work in Section 2 and Section 3.3 sets the range of the relative density ρ between 0.2 to 0.8. The corresponding optimized VSVT structure under 40 × 30 mesh grid, named 'VSVT-1', has a compliance value of 78.7. In comparison, a typical solid structure optimization (where ρ bounds are [0, 1]), such as the SIMP method, can achieve better stiffness performance than the above case, with a computed compliance value of 65.1 (under a 40 × 30 mesh grid). This difference mainly arises from the distinct design domains for the two methods in ρ. Given this situation, we expanded the parameter threshold of ρ in Section 2.2 to [0.2, 1] and then performed a VSVT optimization using the same configuration, named 'VSVT-2'. As a result, the new optimal solution can obtain a solid-porous hybrid structure, which results in a further improved compliance performance of 56.8. These results show consistency with the conclusion drawn by [5], clearly demonstrating the benefits of introducing tunable anisotropy in structural topology optimization.

3.5. 'Full-domain' porous structure design via local volume constraints in VSVT

Local volume constraints are crucial for the optimal design of cellular structures. For example, it is essential to prevent any completely empty regions within the design domain when constructing porous materials for dental fillings. In this scenario, a 'full-domain' porous structure design should be used instead of the 'porous-void hybrid structure', as discussed in the introduction. To meet the above requirement, a global P-norm volume constraint is introduced into our VSVT multi-component optimization in this section, controlling the local material volume $\sum_i \rho_{li} z_{li} > 0$ for each element. The additional constraint, named as g_2, is defined as Eq. (7):

$$g_2: \quad \|\{z_1, z_2, \ldots, z_l, \ldots, z_{N^e}\}\|_n \geq 0.99 \tag{25}$$
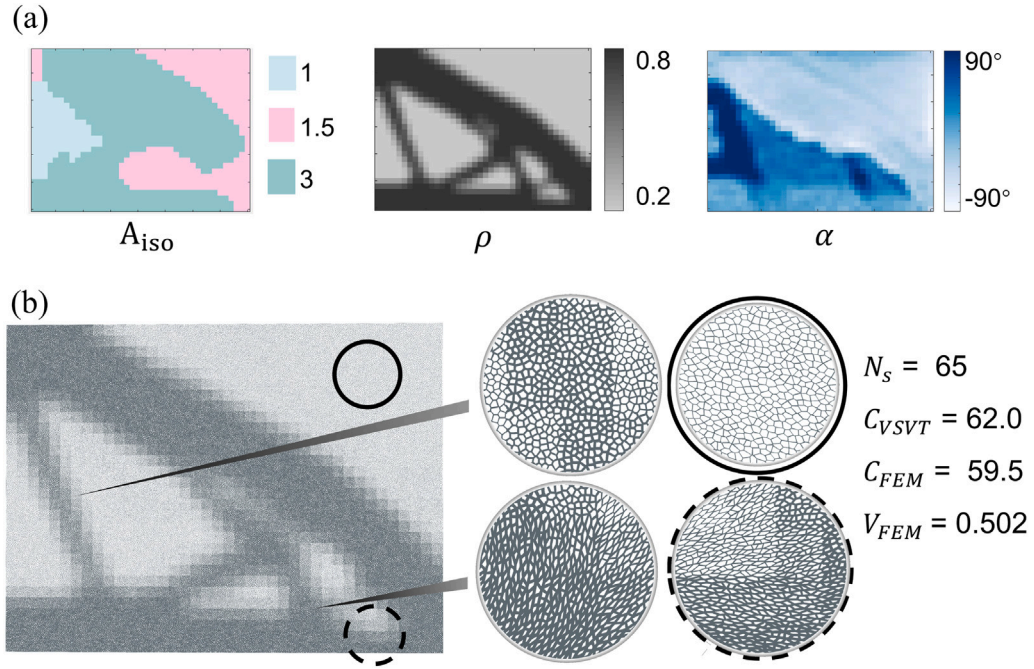
Fig. 13. The VSVT structure design for the MBB case with local volume constraint using the P-norm technique. (a) presents an overview of the final optima for the VSVT structures. (b) present the detailed geometric model for the design. The elements that were completely empty in the original example in Section 3.2, are now filled by the materials with the relative density ρ at least 0.2.

where n is the P-norm parameter, and set to -16 in the work. $\{z_1, z_2, \ldots, z_l, \ldots, z_{N^e}\}$ is a $N^e \times 1$ column vector with terms $z_l = \sum_{i=1}^{m} z_{li}$. With this new constraint, the VSVT structure is compelled to include at least one type of VSVT material in each macro-element during the optimization process, thereby excluding the void macro-element where $Z_l = \mathbf{0}$ as defined in Eq. (8). The final corresponding solutions and structure are shown as Fig. 13.

In overview, the local material volume is determined during the VSVT multi-component optimization process by both the anisotropy index '$\mathbf{Z}$' and relative density 'ρ', rather than solely by ρ as in other topology optimization studies. This implies that the approach decouples the existence of materials in the macroscale element from its relative density variable ρ (or porosity $p = 1 - \rho$). By doing so, the non-existent material regions can be expressed using other variables i.e. $\mathbf{Z}$, and thus avoiding the discontinuity problems due to the sensitivity function of ρ when $\rho = [0, \rho_{min}]$. This approach allows for more flexible and straightforward setting of local volume constraints (either zero or non-zero) in the design domain, enabling the achievement of both 'pores-void hybrid structures' and 'pure porous structures'.

4. Discussions and conclusions

Recently, the Voronoi tessellation technique has been widely used in the design of porous materials and structures to create topological units with isotropic mechanic property and good connectivity, e.g., [10,24,25,50]. In contrast to these research works based on Voronoi tessellation [5,8,32,40], the VSVT method proposed in this work achieves the programmable anisotropy design of topological units through varying Voronoi shapes. This approach allows for the optimization of mechanical properties, particularly stiffness, in multiscale design. Related to other research works on the anisotropy design through typical lattice embedding model [17,26,27], this proposed VSVT approach maintains the smooth connectivity, and produces the topological patterns that closely resemble natural porous materials, such as coral or trabecular bone. In contrast to recent study on anisotropic Voronoi tessellation, which mainly rely on an experimental design approach [33], the VSVT method allows for complete design of porous materials and structures through parametric parameters and provides an efficient optimization framework. Furthermore, the numerical homogenization process offers a thorough and diverse investigation of the mechanical properties of anisotropic Voronoi tessellated structures. The VSVT method and its optimization framework enable the precise design of multiscale porous structures under specific volume constraints.

To achieve an affordable computational cost for the full-scale FEM verification of numerical cases, we only use relative coarse mesh grid of topological units in the optimization. These may induce a relative obvious 'square jagged edges' in the final geometry model. In practical applications, a boundary post-process method following the work [24] is introduced in Appendix C, which allow us to quickly achieve curved boundary. To address this issue completely, an refined, unstructured mesh configuration [40,43] or level-set based implicit boundary representation [26] can be incorporated into the existing VSVT optimization workflow.

In this work, we relax the periodic boundary condition typically used during the homogenization, which is similar to the approach described in [5]. Different from a standard periodic boundary condition (PBC), which requires strict symmetry in material distribution at the boundaries of RVE units [25], our approach aims to maintain high computational accuracy while allowing for natural connectivity and increased design freedom at the topology unit interfaces. The standard PBC method generally imposes symmetrical material distribution and corresponding symmetry of finite element method (FEM) nodes at the RVE boundaries to ensure a consistent strain boundary condition during homogenization. However, in the VSVT method, we do not impose this constraint across RVE boundaries. Instead, as a compensation, we define a lower bound for Voronoi seeds N_s within the RVE domain and employ uniform Poisson disk sampling to ensure a dense and uniformly porous structure within the RVE interior. In doing so, a significant separation of the scale between the micro-Voronoi pores and the macro-RVE is achieved, allowing the global deformation of the VSVT RVE units to adhere to continuity and small deformation mechanics assumptions. As a result, our numerical homogenization errors remain within a narrow, acceptable range. The close agreement between the compliance results of the final realistic FEM model and the homogenized model, as presented in Sections 3.2 and 3.4, demonstrates the accuracy and effectiveness of the VSVT homogenization process, even when the periodic boundary condition is relaxed.

The proposed method is highly accurate and efficient in computation. Regarding the numerical homogenization, the average compliance and volume error between the homogenized model and the detailed FEM model are approximately 6.0% and 1.5%, respectively. This relatively high accuracy is achieved through the appropriately stipulated parameter window of seed amount N_s. A tuned specific surface area distribution example and P-norm local volume constraint example are respectively demonstrated in the paper to support the statements. The de-homogenization process provides extensive design flexibility in VSVT micro-architectures, making the VSVT method suitable for many practical engineering applications, such as energy conversion and storage, thermal management, femoral implants, desalination, and biosensors.

In summary, this work proposes a novel design method for stochastic yet stable porous structures with tunable anisotropy, namely, varied-shape Voronoi tessellation (VSVT). A specialized multi-scale topology optimization framework is implemented to perform the optimal design of bio-inspired advanced materials using the VSVT method. The VSVT method, which applies the modified Riemannian metric in Voronoi construction, is capable of generating porous materials and structures with high natural similarity. Benefiting from the tunable and programmable local anisotropy of VSVT RVE units, the optimization designs of porous structures exhibit superior mechanical performance compared to the isotropic porous structures.

CRediT authorship contribution statement

Zeyang Li: Visualization, Validation, Software, Methodology, Formal analysis, Data curation, Conceptualization. **Zhangming Wu:** Writing – review & editing, Validation, Supervision, Methodology, Conceptualization.

Declaration of competing interest

The authors declare that they have no known competing financial interests or personal relationships that could have appeared to influence the work reported in this paper.

Data availability

Code datas will be available at https://github.com/lizy20.

Acknowledgments

Appendix A. Poisson disk sampling

A Poisson disk sampling pattern is a uniform seed distribution where the points are no closer than a specified distance, r_{min}. In this work, r_{min} has been used as a parameter in codes that control the number of seeds, N_s, in the RVE domain. The most typical Poisson disk sampling method has been applied in many studies is the one proposed by Bridson sampling method [34], for its high efficiency. However, the method is based on a constant minimum distance value r_{min}, which may be inadequate for achieving a more flexible de-homogenization when considering that the number of seeds, N_s, may vary across different macro-elements in the design domain (see example in Section 3.3). Fig. A.1(a) indicates the presence of a boundary coincidence problem in the sequential seeding of each RVE by Bridson's method. In this context, the 'variable-density Poisson disk sampling' method proposed by Nicholas et al. [35] is employed in this paper to circumvent the above drawbacks and achieve a smoothly varying boundary between the two RVEs, as shown in Fig. A.1 (b). The method employs the local Poisson disk parameter r_i instead of the constant r_{min} to define the minimum distance between seed pairs. This allows the seeding process to be completed throughout the design domain in a single iteration, circumventing the issue of 'boundary coincidence'. A packaged open-source Matlab codes 'Dworklib' can be utilized to complete above operation in practical application.
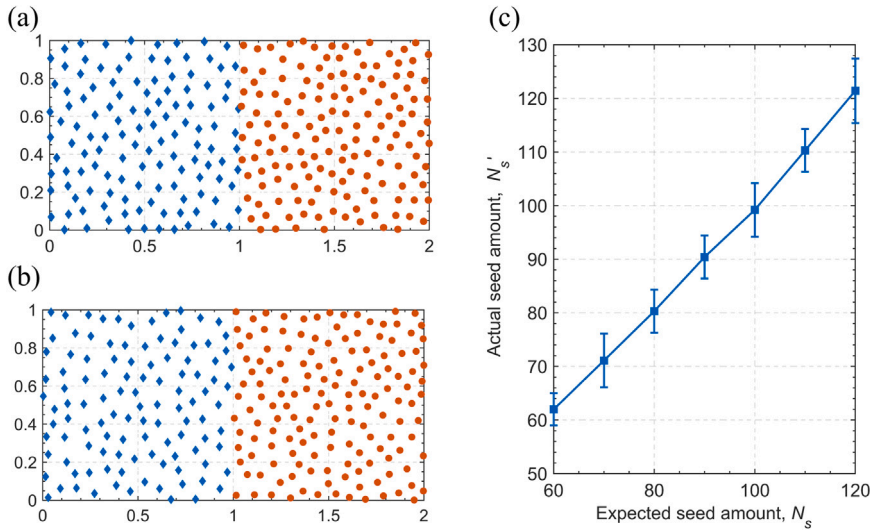
Fig. A.1. The demonstration of two different Poisson disk sampling algorithms and the error in seed amounts during the seeding process. (a), (b) is the seeding pattern of two adjacent RVE elements by 'constant Poisson disk sampling' and 'variable-density Poisson disk sampling' method, respectively. The RVE elements is both in a normalized size while N_s = 120 or 150. A typical points overlapping phenomenon is observed at RVEs' interface in (a) but disappear in (b). Image (c) suggested the errors between actual seed amount N_s' and expected N_s. N_s' is obtained from the 'dworklib' open source codes, where its input r_i is computed by substituting N_s into empirical equation Eq. (A.1). For each error bar, 10 repetitions were performed under identical sampling conditions. The N_s' finally presents good matching relationship to the expected seed amount N_s.

For the sake of clarity and intuition, we used seed amount N_s to describe the seeding density in the manuscript. However, it should be noted that the seed amount N_s cannot be used directly as an input for the 'variable-density Poisson disk sampling' algorithm. Insteadly, it must be transformed into a corresponding input, r_i, within the program. Calculating the mapping function between N_s and r_i is analogous to solving a 'circles packaging' problem. Herein, we provide an estimated equation based on experience to rapidly determine r_i with respect to the expected N_s, as follows,

$$r_i = \frac{L}{\sqrt{2} \cdot \sqrt{\frac{\pi}{4} \cdot N_s}} \tag{A.1}$$

where L and N_s are the actual length and seed density parameter of ith element, respectively. For each expected N_s, we calculated corresponding r_i by Eq. (A.1) and substituted it into 'Dworklib' codes to obtain final Voronoi seeding distribution. The final actual seed amount N_s' may present an error to the expected N_s due to the seeding stochasticity as shown in the Fig. A.1 (c). It can be seen that error is relative small and stay in an acceptable window.

Appendix B. Elasticity of VSVT RVE

The Elasticity tensor function terms $\mathbf{D}^H(A_{iso}, \rho)$ is shown in Fig. B.1. D_{11} shows a smooth increasing trend as ρ or A_{iso} increases, while D_{12}, D_{22}, D_{33} show increasing trends as ρ increase or A_{iso} decreases. The smoothness of function in the image ensures the feasibility of common gradient-based optimization with the continuous function $\mathbf{D}^H(A_{iso}, \rho)$. However, it should be noted that the gradient of the function in regions where $A_{iso} \in [3, 5]$ & $\rho \leq 0.3$ are quite close to 0 and may cause a 'gradient vanishing' problem in the optimization process. Besides, the discussed common method may also show a decreased convergence speed and efficiency compared to the multi-component optimization method used in the manuscript. The abandonment of variable $\mathbf{Z}$ in optimization process also presents a challenge for the method in achieving a 'void-pores hybrid structure' in the design domain, as discussed in Section 3.5. More detailed study of these issues is looking forward in the future.

For the sake of comparison and application, a polynomial fitting function of the homogenized elasticity tensor D^H is also provided here. The coefficient values of the 4th order polynomial fitting function, as $D_{ij} = c_1 \rho^4 + c_2 \rho^3 + c_3 \rho^2 + c_4 \rho + c_5$, are listed in Table B.1. It is notable that the D_{22}, D_{33}, D_{12} is expressed as piecewise functions for a high accuracy. The approximate-zero terms i.e. $D_{13}, D_{23}, D_{31}, D_{32}$ are omitted in the table. The total error between this polynomial function and original database is controlled in a level less than 5%.

Appendix C. Post-processing for optimization

A density filtering method with high filtering radius cannot avoid the material overlapping phenomenon in a multi-material optimization process, such as the 'grey elements' in the black circle in Fig. C.1(a). By applying an additional Heaviside projection to
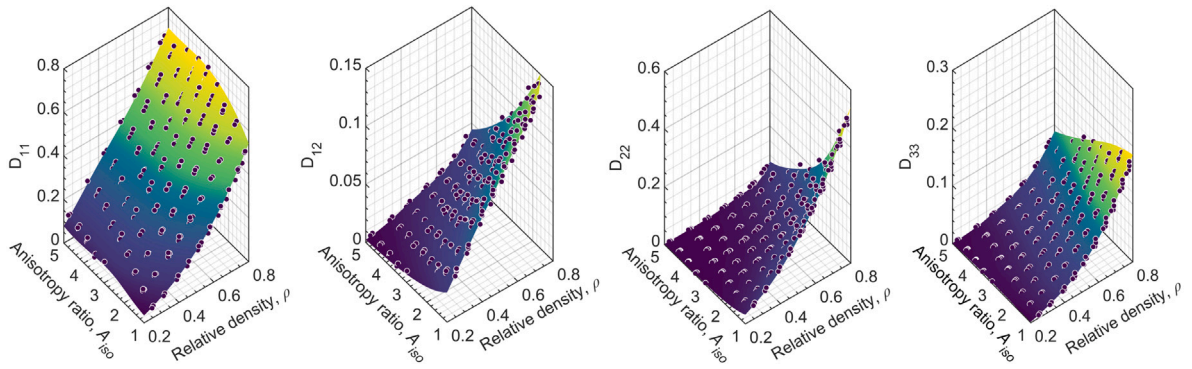
Fig. B.1. The demonstration of Elasticity tensor $\mathbf{D}^H$ with respect to the continuous density variables ρ and A_{iso}. The specific terms approaching zero i.e. D_{13}, D_{23}, are omitted in the figure.

Table B.1
The piecewise polynomial fitting function of the homogenized elasticity tensor D^H with respect to ρ.

D_{11}							D_{22}						
A_{iso}	ρ	c_1	c_2	c_3	c_4	c_5	A_{iso}	ρ	c_1	c_2	c_3	c_4	c_5
1	0.2–0.9	5.0791	−9.7672	7.4556	−1.9437	0.2168	1	0.2–0.6	−2.9339	5.4647	−2.8275	0.9600	−0.0665
								0.6–0.9	−5.7444	24.7264	−33.5769	19.6209	−3.9910
1.5	0.2–0.9	3.5070	−7.1077	5.9462	−1.4027	0.1527	1.5	0.2–0.6	−1.3674	4.0279	−2.4867	0.7737	−0.0727
								0.6–0.9	30.3912	−82.9658	86.1375	−39.0837	6.6117
2	0.2–0.9	1.9262	−3.4763	2.8256	−0.2045	0.0193	2	0.2–0.6	0.5643	0.4657	−0.4132	0.1981	−0.0216
								0.6–0.9	49.9647	−140.0186	148.8563	−70.0330	12.3239
3	0.2–0.9	2.9880	−6.2857	5.2663	−1.0005	0.1205	3	0.2–0.6	1.1529	−0.9365	0.3752	−0.0377	0.0001
								0.6–0.9	81.1213	−229.0232	243.9038	−115.3065	20.3968
4	0.2–0.9	1.9565	−3.8121	3.1859	−0.2794	0.0380	4	0.2–0.7	1.6051	−1.9316	0.9562	−0.1933	0.0141
								0.7–0.9	168.2154	−506.0367	573.5441	−289.4525	54.8331
5	0.2–0.9	1.7100	−3.1146	2.4432	0.0505	−0.0005	5	0.2–0.7	2.8005	−3.5055	1.3816	−0.1303	−0.0073
								0.7–0.9	198.1927	−594.4142	669.7490	−335.3312	62.9017

D_{33}							$D_{12} = D_{21}$						
A_{iso}	ρ	c_1	c_2	c_3	c_4	c_5	A_{iso}	ρ	c_1	c_2	c_3	c_4	c_5
1	0.2–0.6	0.5568	−0.8668	0.8545	−0.2303	0.0309	1	0.2–0.6	−0.4733	1.1036	−0.8702	0.5067	−0.0531
	0.6–0.9	4.6797	−12.6869	13.4843	−6.1958	1.0824		0.6–0.9	5.9893	−15.5484	15.2748	−6.4710	1.0806
1.5	0.2–0.6	−0.0100	0.4438	−0.0941	0.0288	−0.0031	1.5	0.2–0.6	−1.3214	2.3708	−1.4201	0.5346	−0.0478
	0.6–0.9	4.1999	−11.0364	11.4664	−5.0839	0.8369		0.6–0.9	7.4317	−19.3858	19.0532	−8.0995	1.3273
2	0.2–0.6	0.3493	−0.2573	0.3444	−0.0889	0.0081	2	0.2–0.6	−0.1010	0.6952	−0.7129	0.4171	−0.0478
	0.6–0.9	6.7012	−18.5812	20.0412	−9.4445	1.6656		0.6–0.9	13.9475	−38.6652	40.4699	−18.6434	3.2510
3	0.2–0.6	0.2281	0.1045	−0.0676	0.0506	−0.0069	3	0.2–0.6	0.2272	−0.2363	0.1473	0.0389	−0.0056
	0.6–0.9	10.4834	−28.6383	30.0519	−13.9342	2.4205		0.6–0.9	23.1216	−64.8966	68.4573	−31.9505	5.5966
4	0.2–0.7	−0.0153	0.8046	−0.7688	0.2941	−0.0347	4	0.2–0.7	−0.6467	1.4833	−1.0505	0.3486	−0.0357
	0.7–0.9	1.2611	3.5567	−11.2487	9.1978	−2.3830		0.7–0.9	40.8905	−120.8625	134.4113	−66.4431	12.3339
5	0.2–0.7	0.4677	−0.2464	−0.0392	0.0761	−0.0127	5	0.2–0.7	0.5850	−0.8209	0.4343	−0.0579	0.0021
	0.7–0.9	12.6241	−32.5440	31.8940	−13.8065	2.2171		0.7–0.9	59.8363	−182.2707	208.8693	−106.4869	20.3806

the anisotropy index $\mathbf{Z}$ in the optimization, most of the grey elements at the interface of VSVT materials can be largely eliminated. However, even with this, a few optimized $\mathbf{Z}$ may still remain in an intermediate state rather than a convergent 0-1 solution as shown in Eq. (8). For example, a $z_l = [0.3, 0.3, 0.45]$ and $z_{li} = [0.55, 0, 0]$ in final optima may be probably transformed into a 'blank element' $z_l = [0, 0, 0]$ or a 'grey element' $z_l = [1, 0, 0]$ after Heaviside projection, as shown in Fig. C.1(b). To address the above issues, a post-processing step sometimes may be needed to attain more precise solution like Fig. C.1(c). The detailed workflow is shown as Matlab pseudo code as Algorithm 1: First, we set the converged solutions as a new initial guess and re-run 25 iterations of the optimization process solely for $\mathbf{Z}$ with a decreased filter radius $R = 1.1$. This approach eliminates most of 'grey elements' caused by the filter can be eliminated. Next, we replace the Heaviside projection with a direct manual projection to adjust $\mathbf{Z}$, converging towards a precise 0-1 solution. Finally, a further sub-optimization of 25 iterations for the sole ρ variable is conducted to achieve an optimal material distribution that adapts to the updated $\mathbf{Z}$ under the given volume constraint.

Notably, we canceled Heaviside projection (reset $\beta = 1$) in this post-processing step to avoid the 'gradient vanishing' problem. Post-processing is not necessary for most examples, however for the 'full-domain' example in Section 3.5, as its amount of 'grey elements' are usually more than that of 'Void-pores hybrid' example, and so the post processing are relative important. Further, as
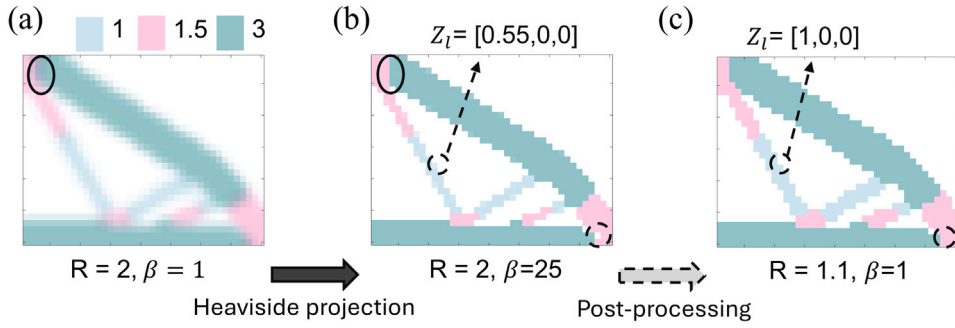
Fig. C.1. The effect of Heaviside projection and post-processing operation in the optimization. It can be seen the material mixing or non-convergence problems are effectively solved by the proposed method. The solid circle notes the problem addressed by 'Heaviside projection', while the dashed one corresponds to that by 'Post-processing'.

the blank macro-element is non-allowed in the final solution in the case, the '0' in Algorithm 1 - 11th row should be correspondingly modified into one type of VSVT material candidate possessing maximum composition in local designated elements.

Algorithm 1 Persuade code for post-processing

1: **Input**: Initialize MMA optimization parameter and load optimized solution ρ and $\mathbf{Z}$.

2: Update density filtering matrix $\mathbf{P}$ with $R = 1.1$; Set $\beta = 1$, *loops* = 1;

3: **while** $loops \leq 25$ **do**

4:      Sub-optimization for $\mathbf{Z}$;

5:      *loops*=*loops*+1.

6: **end while**

7: Do the **manual projection**:

8:      $[\mathbf{M}, \mathbf{idk}]$ = Sum($\mathbf{Z}$,2) $\rightarrow$ Abstract the Maximum value $\mathbf{M}$ and index $\mathbf{idk}$ of row vector

9:                        $Z_l = [z_{l1}, z_{l2}, ..., z_{li}, ..., z_{lm}]$. $\mathbf{M},\mathbf{idk}$ are both $\mathbf{N^e} \times 1$ size column vectors.

10:      $\mathbf{Z}$ = 0*$\mathbf{Z}$; $\mathbf{Z}$(:,$\mathbf{idk}$)=1; $\rightarrow$ z_{li} terms in $\mathbf{Z}_l$ are projected to strict 0-1 solution.

11:      $\mathbf{Z}(\mathbf{M} \leq 0.5,:)=\mathbf{0}$ $\rightarrow$ Elements that $\mathbf{Z}_l$ close to 0 are set as empty.

12: *loops*=0

13: **while** $loops \leq 25$ **do**

14:      Sub-optimization for ρ; $\rightarrow$ The updated $\mathbf{Z}$ causes the material volume constraint g to be changed. By further optimizing the ρ, the VSVT structure will strictly converges to the predefined volume fraction V_{frac}.

15:      *loops*=*loops*+1.

16: **end while**

17: **Output**: $\mathbf{z}, \rho$.

In this work, we used a relatively coarse mesh grid configuration to design VSVT porous structures for cases presented in Section.3, for the purpose of maintaining affordable computation costs of the FEM model during verification process. However, this may cause a "square jagged edges" issue in the final solution as shown in Fig. C.2 (a), affecting on the practical applications. On one hand, this problem can be addressed by incorporating an advanced level-set boundary representation technique into the proposed VSVT topology framework, following the work in [26]. On the other hand, a simple geometry post-processing technique using Boolean cutting, as described in [24], can also solve this issue, effectively. Firstly, the original optimal solutions with jagged boundaries such as A_{iso} shown in Fig. C.2 (a) are manually modified by a typical Path-Smoothing method, achieving curved outer boundary as shown in Fig. C.2 (b). A few local empty region will be filled with solutions from its neighbor units during this process. Then, the cutting domain ϕ_B and modified geometric mapping function $\phi'(\mathbf{x})$ are defined as follows:

$$\begin{cases} \phi_B(\mathbf{x}) = 1, & \mathbf{x} \in B_d \\ \phi_B(\mathbf{x}) = 0, & \mathbf{x} \notin B_d \end{cases} \tag{C.1}$$

$$\phi'(\mathbf{x}) = \phi_B(\mathbf{x}) \cdot \phi(\mathbf{x}) \tag{C.2}$$

where $\phi(\mathbf{x})$ is the original VSVT geometric mapping function as defined in Eq. (4), the final VSVT geometry domain is defined as $\Omega' = \{\mathbf{x}|\phi'(\mathbf{x}) > 0\}$. After de-homogenization process, the final tailored geometry model under MBB-$V_{frac} = 0.3$ configuration is shown in Fig. C.2(c). The "jagged egdes" issue shows effective resolution, and the practical compliance value slightly increase from original 82.7 to 87.5.
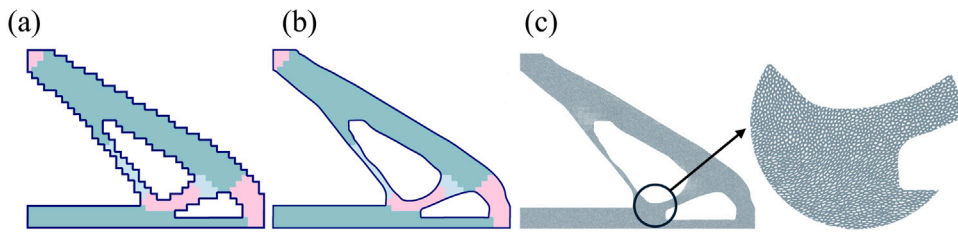
Fig. C.2. The demonstration for boundary post-process by Boolean cutting. (a) the original optimal solution for A_{iso} with jagged boundary. (b) the modified solution for A_{iso} with curved boundary. (c) the new geometry model based on (b). The close-up suggests a disappearance of jagged edges at boundary.
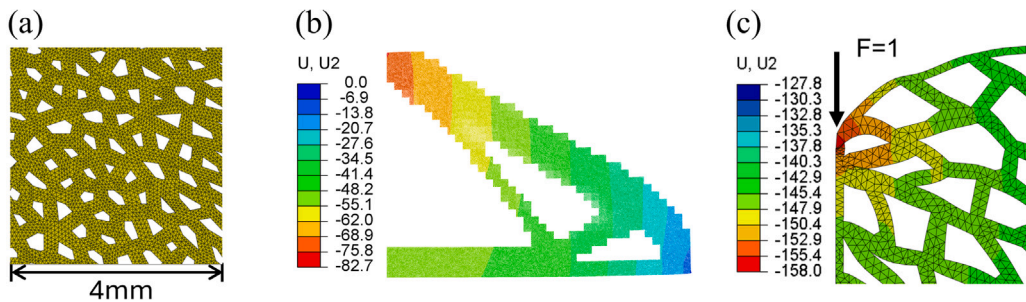

Fig. D.1. The FE model of VSVT porous structure. (a) the illustration of mesh density in one RVE region; (b) the computed result of de-homogenized MBB example with 'N_s' = 50. (c) an example for 'local heavy distortion' problem of loading element.

Appendix D. FEM computation for de-homogenized VSVT structure

The detailed FEM analysis for the VSVT porous structures are carried out in ABAQUS to verify the compliance values obtained by TO optimization in Section 3.4. The meshed model of VSVT structures is achieved by 'Im2mesh' toolbox in Matlab and refined by 'Materialise magic' software (ver. 20). The mesh type is 'CPS3' TRI mesh with refined average size of 0.1 mm, as depicted by Fig. D.1 (a). The total elements of numerical examples in Section 3 is about 1 to 5 millions per case. Note, almost all FEM-computed compliance values show an obvious increasing trend as meshing size becoming refiner in this work. In fact, since we are transforming a typical multi-scale problem into a single-scale one, even using the 0.1 mm mesh density cannot always be small enough to obtain an absolutely accurate result according to our test, especially for the uni-compression loading cases. However, this accuracy has reached the upper limitation of our computing equipment (AMD Ryzen 5795WX-32 cores, RAM 64G). Considering the error by 0.1 mm is already in a relatively small range (FEM result variation is about $[-2\%, 4\%]$ when 0.1 mm decreases to 0.075 mm), we consider the FEM results given by the 0.1 mm mesh size are accurate enough in this work.

For the equivalent comparison with optimization result, the compliance value for FE model is computed as $C_{FEM} = u_l \cdot f_l$, where u_l is the displacement of the loading node, f_l is the value of external loading. Fig. D.1 (b) shows the displacement contour of MBB case in Fig. 11. In addition, a heavy elemental distortion problem may occur at the loading region for partial VSVT geometry models if the truss thickness is relatively thin, as depicted in Fig. D.1 (c). For these cases, an average displacement value of neighboring nodes (within 2 mm radius range of loading node in this work) are calculated as u_l for more accurate and fair comparison with homogenized TO model.

Appendix E. Supplementary data

Supplementary material related to this article can be found online at https://doi.org/10.1016/j.cma.2024.117378.

References

[1] W. Deng, S. Kumar, A. Vallone, D.M. Kochmann, J.R. Greer, Ai-enabled materials design of non-periodic 3d architectures with predictable direction-dependent elastic properties, Adv. Mater. (2024) 2308149.
[2] T.D. Bennett, F.-X. Coudert, S.L. James, A.I. Cooper, The changing state of porous materials, Nature Mater. 20 (9) (2021) 1179–1187.
[3] H. Wang, X. Wang, M. Li, L. Zheng, D. Guan, X. Huang, J. Xu, J. Yu, Porous materials applied in nonaqueous Li–O2 batteries: status and perspectives, Adv. Mater. 32 (44) (2020) 2002559.
[4] S.S. Hoseini, A. Seyedkanani, G. Najafi, A.P. Sasmito, A. Akbarzadeh, Multiscale architected porous materials for renewable energy conversion and storage, Energy Storage Mater. (2023) 102768.
[5] F.V. Senhora, E.D. Sanders, G.H. Paulino, Optimally-tailored spinodal architected materials for multiscale design and manufacturing, Adv. Mater. 34 (26) (2022) 2109304.
[6] J. Ying, L. Lu, L. Tian, X. Yan, B. Chen, Anisotropic porous structure modeling for 3d printed objects, Comput. Graph. 70 (2018) 157–164.

[7] J.J. Kim, J. Nam, I.G. Jang, Computational study of estimating 3d trabecular bone microstructure for the volume of interest from ct scan data, Int. J. Numer. Methods Biomed. Eng. 34 (4) (2018) e2950.

[8] J. Wu, O. Sigmund, J.P. Groen, Topology optimization of multi-scale structures: a review, Struct. Multidiscip. Optim. 63 (2021) 1455–1480.

[9] J.J. Kim, I.G. Jang, Image resolution enhancement for healthy weight-bearing bones based on topology optimization, J. Biomech 49 (13) (2016) 3035–3040.

[10] S. Lin, N. Chou, G. Li, D. Bao, Y. Cai, Y.M. Xie, G. Wang, A gradient-evolutionary coupled topology optimization for sheet reinforcement based on the mechanics of voronoi pattern on dragonfly wings, Adv. Eng. Softw. 190 (2024) 103600.

[11] D. Li, W. Liao, N. Dai, Y.M. Xie, Anisotropic design and optimization of conformal gradient lattice structures, Comput. Aided Des. 119 (2020) 102787.

[12] M.A. Ali, M. Shimoda, Toward multiphysics multiscale concurrent topology optimization for lightweight structures with high heat conductivity and high stiffness using matlab, Struct. Multidiscip. Optim. 65 (7) (2022) 207.

[13] M.-N. Nguyen, V.-N. Hoang, D. Lee, Multiscale topology optimization with stress, buckling and dynamic constraints using adaptive geometric components, Thin-Walled Struct. 183 (2023) 110405.

[14] J. Gao, X. Cao, M. Xiao, Z. Yang, X. Zhou, Y. Li, L. Gao, W. Yan, T. Rabczuk, Y.-W. Mai, Rational designs of mechanical metamaterials: Formulations, architectures, tessellations and prospects, Mater. Sci. Eng. R 156 (2023) 100755.

[15] J. Gao, H. Xue, L. Gao, Z. Luo, Topology optimization for auxetic metamaterials based on isogeometric analysis, Comput. Methods Appl. Mech. Engrg. 352 (2019) 211–236.

[16] M.P. Bendsøe, N. Kikuchi, Generating optimal topologies in structural design using a homogenization method, Comput. Methods Appl. Mech. Engrg. 71 (2) (1988) 197–224.

[17] E. Sanders, A. Pereira, G. Paulino, Optimal and continuous multilattice embedding, Sci. Adv. 7 (16) (2021) eabf4838.

[18] M.P. Bendsøe, Optimal shape design as a material distribution problem, Struct. Optim 1 (1989) 193–202.

[19] A. Bhatia, A.K. Sehgal, Additive manufacturing materials, methods and applications: A review, Mater. Today: Proc 81 (2023) 1060–1067.

[20] R. Christensen, Mechanics of low density materials, J. Mech. Phys. Solids 34 (6) (1986) 563–578.

[21] Z. Hashin, S. Shtrikman, A variational approach to the theory of the elastic behaviour of multiphase materials, J. Mech. Phys. Solids 11 (2) (1963) 127–140.

[22] E. Andreassen, C.S. Andreasen, How to determine composite material properties using numerical homogenization, Comput. Mater. Sci. 83 (2014) 488–495.

[23] H. Lu, T.-U. Lee, J. Ma, D. Chen, Y.M. Xie, Designing 2d stochastic porous structures using topology optimisation, Compos. Struct. 321 (2023) 117305.

[24] Q.T. Do, C.H.P. Nguyen, Y. Choi, Homogenization-based optimum design of additively manufactured voronoi cellular structures, Addit. Manuf. 45 (2021) 102057.

[25] L. Chen, Y. Pan, X. Chu, H. Liu, X. Wang, Multiscale design and experimental verification of voronoi graded stochastic lattice structures for the natural frequency maximization problem, Acta Mech. Sin 39 (8) (2023) 422445.

[26] J. Gao, Z. Luo, H. Li, L. Gao, Topology optimization for multiscale design of porous composites with multi-domain microstructures, Comput. Methods Appl. Mech. Engrg. 344 (2019) 451–476.

[27] M. Fujioka, M. Shimoda, M. Al Ali, Concurrent shape optimization of a multiscale structure for controlling macrostructural stiffness, Struct. Multidiscip. Optim. 65 (7) (2022) 211.

[28] C.F. Christensen, F. Wang, O. Sigmund, Topology optimization of multiscale structures considering local and global buckling response, Comput. Methods Appl. Mech. Engrg. 408 (2023) 115969.

[29] C. Pan, Y. Han, J. Lu, Design and optimization of lattice structures: A review, Appl. Sci. 10 (18) (2020) 6374.

[30] M. Zhao, X. Li, D.Z. Zhang, W. Zhai, Tpms-based interpenetrating lattice structures: design, mechanical properties and multiscale optimization, Int. J. Mech. Sci. 244 (2023) 108092.

[31] C. Zhang, T. Wu, S. Xu, J. Liu, Multiscale topology optimization for solid–lattice–void hybrid structures through an ordered multi-phase interpolation, Comput. Aided Des. 154 (2023) 103424.

[32] L. Zheng, S. Kumar, D.M. Kochmann, Data-driven topology optimization of spinodoid metamaterials with seamlessly tunable anisotropy, Comput. Methods Appl. Mech. Engrg. 383 (2021) 113894.

[33] B. Liu, S. Li, W. Cao, W. Lu, P. Lu, Design of 3d anisotropic voronoi porous structure driven by stress field, Comput. Methods Appl. Mech. Engrg. 420 (2024) 116717.

[34] R. Bridson, Fast Poisson disk sampling in arbitrary dimensions, SIGGRAPH Sketches 10 (1) (2007) 1.

[35] N. Dwork, C.A. Baron, E.M. Johnson, D. O'Connor, J.M. Pauly, P.E. Larson, Fast variable density Poisson-disc sample generation with directional variation for compressed sensing in mri, Magn. Reson. Imaging 77 (2021) 186–193.

[36] H. Zhong, T. Song, C. Li, R. Das, J. Gu, M. Qian, The gibson-ashby model for additively manufactured metal lattice materials: Its theoretical basis, limitations and new insights from remedies, Curr. Opin. Solid State Mater. Sci. 27 (3) (2023) 101081.

[37] M.P. Bendsøe, O. Sigmund, Material interpolation schemes in topology optimization, Arch. Appl. Mech 69 (1999) 635–654.

[38] C. Lu, M. Hsieh, Z. Huang, C. Zhang, Y. Lin, Q. Shen, F. Chen, L. Zhang, Architectural design and additive manufacturing of mechanical metamaterials: A review, Engineering 17 (2022) 44–63.

[39] H. Deng, Y. Huang, S. Wu, Y. Yang, Binder jetting additive manufacturing: Three-dimensional simulation of micro-meter droplet impact and penetration into powder bed, J. Manuf. Process. 74 (2022) 365–373.

[40] E.D. Sanders, M.A. Aguiló, G.H. Paulino, Multi-material continuum topology optimization with arbitrary volume and mass constraints, Comput. Methods Appl. Mech. Engrg. 340 (2018) 798–823.

[41] B. Yi, G.H. Yoon, X. Peng, A simple density filter for the topology optimization of coated structures, Eng. Optim. 53 (12) (2021) 2088–2107.

[42] S. Dou, A projection approach for topology optimization of porous structures through implicit local volume control, Struct. Multidiscip. Optim. 62 (2) (2020) 835–850.

[43] E.D. Sanders, A. Pereira, M.A. Aguiló, G.H. Paulino, Polymat: an efficient matlab code for multi-material topology optimization, Struct. Multidiscip. Optim. 58 (2018) 2727–2759.

[44] D. Chen, K. Gao, J. Yang, L. Zhang, Functionally graded porous structures: Analyses, performances, and applications–a review, Thin-Walled Struct. 191 (2023) 111046.

[45] J. Zhao, C. Wang, Robust topology optimization under loading uncertainty based on linear elastic theory and orthogonal diagonalization of symmetric matrices, Comput. Methods Appl. Mech. Engrg. 273 (2014) 204–218.

[46] E.M. Sussman, M.C. Halpin, J. Muster, R.T. Moon, B.D. Ratner, Porous implants modulate healing and induce shifts in local macrophage polarization in the foreign body reaction, Ann. Biomed. Eng 42 (2014) 1508–1516.

[47] A. Bagheri, I. Buj-Corral, M. Ferrer Ballester, M. Magdalena Pastor, F. Roure Fernandez, Determination of the elasticity modulus of 3d-printed octet-truss structures for use in porous prosthesis implants, Materials 11 (12) (2018) 2420.

[48] Q. Zhou, K. Zhu, J. Li, Q. Li, B. Deng, P. Zhang, Q. Wang, C. Guo, W. Wang, W. Liu, Leaf-inspired flexible thermoelectric generators with high temperature difference utilization ratio and output power in ambient air, Adv. Sci. 8 (12) (2021) 2004947.

[49] Y. Li, W. Li, T. Han, X. Zheng, J. Li, B. Li, S. Fan, C.-W. Qiu, Transforming heat transfer with thermal metamaterials and devices, Nat. Rev. Mater. 6 (6) (2021) 488–507.

[50] H. Liu, L. Chen, Y. Jiang, D. Zhu, Y. Zhou, X. Wang, Multiscale optimization of additively manufactured graded non-stochastic and stochastic lattice structures, Compos. Struct. 305 (2023) 116546.